AD_________________

Award Number: W81XWH-07-1-0324

TITLE: Quantitative Digital Tomosynthesis Mammography for Improved Breast Cancer Detection and Diagnosis

PRINCIPAL INVESTIGATOR: Yiheng Zhang, Ph.D.

CONTRACTING ORGANIZATION: University of Michigan
Ann Arbor, Michigan 48109

REPORT DATE: April 2008

TYPE OF REPORT: Annual Summary

PREPARED FOR: U.S. Army Medical Research and Materiel Command
Fort Detrick, Maryland 21702-5012

REPORT DOCUMENTATION PAGE

Form Approved OMB No. 0704-0188

1. REPORT DATE	2. REPORT TYPE	3. DATES COVERED
30-04-2008	ANNUAL SUMMARY	1 APR 2007 - 31 MAR 2008

4. TITLE AND SUBTITLE
Quantitative Digital Tomosynthesis Mammography for Improved Breast Cancer Detection and Diagnosis

5a. CONTRACT NUMBER

5b. GRANT NUMBER
W81XWH-07-1-0324

5c. PROGRAM ELEMENT NUMBER

6. AUTHOR(S)
Yiheng Zhang, Ph.D.

Email: yihzhang@med.umich.edu

5d. PROJECT NUMBER

5e. TASK NUMBER

5f. WORK UNIT NUMBER

7. PERFORMING ORGANIZATION NAME(S) AND ADDRESS(ES)

University of Michigan
Ann Arbor, Michigan 48109

8. PERFORMING ORGANIZATION REPORT NUMBER

9. SPONSORING / MONITORING AGENCY NAME(S) AND ADDRESS(ES)
U.S. Army Medical Research and Materiel Command
Fort Detrick, Maryland 21702-5012

10. SPONSOR/MONITOR'S ACRONYM(S)

11. SPONSOR/MONITOR'S REPORT NUMBER(S)

12. DISTRIBUTION / AVAILABILITY STATEMENT
Approved for Public Release; Distribution Unlimited

13. SUPPLEMENTARY NOTES

14. ABSTRACT
The goal of the project is to develop advanced Digital Tomosynthesis Mammography (DTM) reconstruction algorithms with artifact reduction methods to optimize image quality and minimize image artifacts, and to improve quantitative linear attenuation coefficient estimation of breast tissues. When fully developed, the DTM can provide radiologists improved quantitative, three-dimensional volumetric information of the breast tissue, and assist in breast cancer detection and diagnosis.
During this project year, we have performed the following tasks: (1) implementation and comparison of multiple algorithms for limited-angle cone-beam tomography in DTM reconstruction, and development of dedicated breast phantom and image quality evaluation measures, (2) development of efficient algorithm for iterative DTM reconstruction method by utilization of breast shape information, (3) development of artifact reduction methods to remove image artifacts from multiple sources, and (4) investigation of the impact of DTM system and imaging condition parameters on the reconstructed image quality.
In summary, we have completed a number of studies in the development of advanced reconstruction algorithms for DTM. We have made progress in two tasks proposed in the project. We have found that our advanced reconstruction algorithms can provide improved reconstructed DTM image quality with minimized artifacts. We will continue the development of scatter correction and beam hardening correction methods in DTM reconstruction algorithms to improve the quantitative estimation of the linear attenuation properties of breast tissue in the coming years.

15. SUBJECT TERMS

Digital Tomosynthesis Mammography (DTM), image reconstruction, artifact reduction, image quality

16. SECURITY CLASSIFICATION OF: a. REPORT	b. ABSTRACT	c. THIS PAGE	17. LIMITATION OF ABSTRACT	18. NUMBER OF PAGES	19a. NAME OF RESPONSIBLE PERSON
U	U	U	UU	59	USAMRMC
					19b. TELEPHONE NUMBER *(include area code)*

Table of Contents

Introduction

Digital Tomosynthesis Mammography (DTM) is one of the most promising techniques that can provide quasi three-dimensional (3D) information of the breast and potentially improve early detection of breast cancers. The development of the DTM system is still at its early stage and current image reconstruction methods result in DTM images with strong artifacts due to the limited-angle data. Moreover, current methods cannot reconstruct linear attenuation coefficients (LACs) accurately due to scatter and beam-hardening artifacts. The goal of our project is to conduct studies to develop advanced DTM reconstruction algorithms to optimize image quality and minimize image artifacts, as well as to improve quantitative LAC estimation of breast tissues. We will focus on the evaluation of effects of improved reconstruction algorithms on mass lesions although the improved image quality should benefit the detection and diagnosis of microcalcifications as well. The following specific aims will be addressed in the three-year period of the project: (1) Quantitative comparison of several algorithms for 3D limited-angle cone-beam tomographic problem in breast tomosynthesis mammography. (2) Development of artifact reduction methods to suppress multiple sources of artifacts that affect image quality and the quantitative estimation of LACs. (3) Development of scatter and beam hardening correction methods and further improve the image quality and the quantitative estimation of LACs in DTM. (4) Evaluation of the detection accuracy of mass lesions and the classification accuracy between malignant and benign masses with and without the proposed correction methods using collected patient data and computer-aided detection (CADd) and diagnosis (CADx) systems being developed in our laboratory.

Body

This is the first year annual report of our project. In the project period (4/1/07-3/31/08), we have conducted a number of studies in Digital Tomosynthesis Mammography (DTM), including implementation and comparison of multiple reconstruction algorithms, development of dedicated breast phantom and performance measures for image quality evaluation, development of breast-shape guided efficient algorithm for iterative reconstruction method, development of artifact reduction methods to suppress DTM image artifacts from multiple sources, and investigation of the impact of DTM imaging conditions on image quality.

(A) Implementation and comparison of multiple algorithms for limited-angle cone-beam tomography in DTM reconstruction, and development of dedicated breast phantom and image quality evaluation measures.

In DTM, a sequence of low-dose projection-view images is acquired from a limited angular range while the total dose is set to be comparable to that of regular mammography. The reconstruction of the 3D breast volume from 2D projection images therefore represents a limited-angle cone-beam tomographic problem. We have implemented most of the representative algorithms and have quantitatively compared three methods based on dedicated breast phantom studies and image quality evaluation measures.

Method:

For DTM reconstruction or equivalently a limited-angle cone-beam tomographic problem, existing reconstruction methods can be coarsely divided into four categories: back-projection algorithms, transform algorithms, algebraic reconstruction techniques, and statistical reconstruction algorithms. We have implemented most of the representative algorithms, as listed in the following:

- Back-projection algorithms: Shift-and-Add (SAA) method, back-projection (BP) method
- Transform algorithms: FDK filtered back-projection method
- Algebraic reconstruction techniques: algebraic reconstruction technique (ART), simultaneous algebraic reconstruction technique (SART) and simultaneous iterative reconstruction technique (SIRT)
- Statistical reconstruction algorithms: maximum likelihood method with gradient algorithm (ML-Gradient) and maximum likelihood method with convex algorithm (ML-Convex)

We have investigated the impact of a number of factors, including initialization, number of iteration, relaxation parameter and PV image accessing strategy, on the reconstructed image quality of SART. For forward projection calculation in DTM, we have developed a ray-driven model in computing the path-length of a primary x-ray intersecting each voxel with the imaged volume lattice.

We have developed a number of dedicated breast phantoms in image quality evaluation. The breast phantoms include simulated masses with different contrasts, simulated microcalcification clusters, high-contrast metal wires to simulate metal markers or biopsy clips, and low-contrast plastic wires to simulate mass speculations. The test objects are distributed in different regions and depths, of which some are overlapped each other. Other phantoms include breast-shape slabs consisted of breast-tissue-equivalent materials, i.e. heterogeneous mixture of fibroglandular-tissue-mimicking material. We have acquired a large number of DTM images of these phantoms, as well as ACR (the American College of Radiology) mammography accreditation phantom with a GE prototype DTM system installed at the University of Michigan Hospital. This system has a CsI phosphor/a:Si active matrix flat panel digital detector with a pixel size of 0.1 mm×0.1 mm and the raw image data are 16 bits. For tomosynthesis imaging, the x-ray tube is automatically rotated in 3° increments to acquire projection images at 21 different angles over a 60º angular range in less than 8 seconds. The digital detector is stationary during image acquisition. The DTM system uses an Rh-target/Rh-filter x-ray source for all breast thicknesses and no anti-scatter grid is used.

We developed and implemented a number of performance measures in quantitative evaluation of DTM image quality. These measures include the contrast-to-noise ratio, normalized line profiles of test objects, depth resolution, intra-plane spatial resolution, inter-plane artifact spread function, noise power spectrum, edge sharpness measure, and uniformity measure.

Result:

All reconstruction methods that we implemented can reconstruct the features in their correct layers and separate superimposed phantom structures along the Z direction, provided that accurate DTM system geometry is available. Our comparative study of multiple representative algorithms suggested that the two iterative methods, SART and ML-Convex, both can provide high-quality reconstruction DTM images in terms of the performance measures, and are effective in improving the conspicuity of

object details and suppressing inter-plane blurring. The SART method can provide comparable tomosynthesized image quality to those of ML-Convex method but with fewer number of iterations.

For SART method, we have found the suitable combinations of the number of iterations and the relaxation parameter based on both quantitative analysis of image quality measures and visual comparison of reconstructed image quality for a given type of cases. For initialization of the SART method, both a constant distribution and a BP reconstructed volume have been evaluated. It is also found that the SART method is robust with respect to PV access ordering. In addition, for such a limited-angular range and a limited number of acquired PV images in DTM, we have found that the order-subset strategy, which groups selected part of the PVs images together in updating the volume following a specific order, did not give any advantage in DTM reconstruction, although it is frequently used in statistical reconstruction methods for other full-angle imaging modalities.

Conclusion:

The SART method can provide high-quality reconstruction images for DTM. The reconstruction parameters of SART have to be further investigated and optimized when the system design and/or the imaging conditions change.

(B) Development of efficient algorithm for iterative DTM reconstruction method by utilization of breast shape information

Iterative method such as SART can produce good tomosynthesized image quality compared to maximum likelihood type algorithms. However, the computational burden of iterative methods is the major concern in future clinical practice of DTM. In this study, we have developed methods to incorporate both 2D and 3D breast boundary information within the SART reconstruction algorithm to improve the efficiency of DTM reconstruction. This will also address the problem of boundary artifacts.

Method:

The 2D breast boundary on a PV image is segmented by a breast boundary detection program developed in our laboratory and adapted to suit DTM application. Two main steps were in the algorithm, including detection of an initial breast boundary by applying Otsu's thresholding method to the histogram of the input image and performance of a breast boundary tracking procedure based on the initial boundary and gradient information from both horizontal and vertical Sobel filtering. With the detected 2D breast boundary curves on all PV images, we developed a "3D conical trimming" method to generate a 3D breast surface within the imaged volume and enclose the compressed breast while excluding the exterior air space. This method restore the unique convex hull inside the 3D imaged volume assigned to the DTM system by reconstruction modeling of which the projections at different angles precisely correspond to the breast shadow on each PV image. The convex hull combined with the top and bottom surfaces of the breast delineated by the compression paddle and the breast support plate define an enclosed breast volume.

We developed an efficient implementation of the SART method based on the breast boundary information. First, when the imaged volume is updated by each PV image in the SART iterative process, the re-projection and the back-projection of the difference between the calculated data and the measured data will only be performed

along those “valid” rays within the 2D breast area. All rays outside the 2D breast area will be ignored without any manipulation. Second, after one complete SART iteration has been performed, i.e. all PV images have been used exactly once in updating the imaged volume, the 3D breast surface is used to mask the resulting volume and set the values of all voxels outside the breast surface to that of air.

Result:

This method substantially reduced the computational effort compared to full-field processing by eliminating the processing of all rays outside the breast region on each individual PV. The saving in computation time depends on the breast size and breast position of each patient case that will affect the percentage of the breast area with respect to the full-field dimension on PV images. Therefore, the reduction in computation time is more for small breasts. The application of the 3D breast surface, generated from all detected 2D breast boundaries, to the reconstructed slices removed all breast boundary artifacts. With the 2D breast mask information incorporated, the detector boundary artifacts outside the breast have been eliminated. In addition, the skin-lines in all DTM images are less over-enhanced when the reconstruction is limited to the valid rays within the 2D breast boundary. The skin-thickening artifact of the original SART method is due to edge enhancement by the reconstruction algorithm: the inside part of breast area is updated and the outside part is fit to the background noise measurement, and the difference will be enhanced iteratively. In contrast, with 2D breast mask information, only one side within the breast boundary has been updated while the outside voxels maintain their initialized values, therefore the edge enhancement effect of the SART method will be less amplified by multiple updates from the different PVs.

Conclusion:

In this study, we have applied the 2D breast boundary information and the generated 3D breast surface to SART reconstruction in breast tomosynthesis mammography. The 2D breast boundary is detected on the projection view images using a boundary tracking algorithm developed in our laboratory and the 3D breast surface is generated with a 3D conical trimming method. The 2D breast boundary curves on PV images are used to restrict the SART reconstruction to be performed only inside the breast area while the 3D breast surface is used to exclude reconstruction artifacts outside the breast volume. Experimental results with patient PV images demonstrated that the proposed method can substantially improve computational efficiency by eliminating unnecessary reconstruction in regions outside the breast. Both breast boundary and detector boundary artifacts can be effectively removed by the proposed method.

(C) Development of artifact reduction methods to remove image artifacts from multiple sources

Due to the finite size of the flat-panel detector and the limited field of view, DTM reconstruction contains artifacts caused by the truncated projection-view (PV) images. In this study, we have developed methods to remove two types of truncation artifacts: detector boundary discontinuity and underestimation of the attenuation pathlength due to the preset imaged volume in reconstruction modeling. Both of these truncation artifacts are apparent mainly at the image boundary of DTM slices. They will obscure the breast tissue details near the boundary of DTMs, potentially affecting the accuracy of lesion

detection. We have developed correction techniques to reduce their visibility and recover the obscured breast tissue details. A custom-built breast phantom plus a variety of image quality measures were developed to quantitatively evaluate the improvements. The proposed methods have been also applied to DTM patient cases.

Method:

When a portion of the breast is not recorded in some or all of the PV images because of a finite-size detector, the truncated projections will cause artifacts in DTM reconstruction. The limited field of view (FOV) results in unexposed regions in the imaged volume and truncation of the PVs, particularly at large projection angles. In iterative reconstruction such as SART, the imaged volume is updated by processing each individual PV image, i.e. only the part of the imaged volume within the cone-beam ray path of the current PV will be updated. This will result in discontinuity in the voxel values across the cone-beam path boundary which will be enhanced by further PV processing in the same and subsequent iterations. These artifacts, referred to as “detector boundary” truncation artifacts, appear as bright staircase-like lines or bands at the two sides perpendicular to the x-ray source motion on all tomosynthesized slices. A local intensity-equalization method was developed to suppress the discontinuity of the reconstructed voxel intensity. Specifically, for each PV image, after the updating using the current PV is completed, we replace all voxel values within the oblique wedge-shape volume with some average values obtained from their neighborhood region.

A second source of truncation artifacts is caused by the missed portion of breast tissue that is outside the finite imaged volume modeled in the reconstruction algorithm. The missed tissue volume will cause estimation error in the x-ray attenuation. Since the attenuation will be considered to have occurred only within the shortened pathlength, the voxel values will be overestimated. The overestimated attenuation results in bright voxels and will be referred to as “glaring” artifact. For any x-ray incident on the preset rectangular imaged volume from the boundary side, it is assumed that this ray has encountered very large attenuation if the corresponding detected x-ray intensity is below a predetermined threshold. The computed total attenuation of this ray will be compensated for by assuming that the missing volume is filled with “average” breast tissue. In addition, the modified difference between the detected data and the new computed data is normalized by the compensated total pathlength but back-projected only to those voxels within the preset imaged volume.

A custom-built breast phantom was developed for quantitative evaluation of the artifact reduction. The phantom contains test objects including simulated masses with different contrast, high-contrast metal wires to simulate metal markers or biopsy clips, and low-contrast plastic wires to simulate spiculations. The test objects were arranged in groups in both the boundary and middle regions and the phantom was placed at various locations with respect to the stationary detector such that the imaged objects in the boundary area were truncated in varying number of PVs. Placing the breast phantom at the various locations enables the investigation of the effectiveness of the artifact reduction methods for different degrees of PV truncation. In addition to the contrast-to-noise ratio (CNR) and the normalized line profiles of feature objects, a non-uniformity error index was introduced to evaluate the reconstructed image quality of homogeneous Lucite background without and with the proposed artifact reduction methods.

Result:

Results of breast phantom study have demonstrated that the proposed methods enhanced the overall reconstructed image quality of the truncated regions, resulting in much smoother reconstructed distributions. Substantial increases in CNR values of the test objects and in the uniformity of the reconstructed homogeneous Lucite background were also obtained. The improved boundary image areas gained comparable quality to that in the central region of view where no PV truncation occurred. The artifact reduction methods do not affect the sharpness of the line profiles of high-density objects. For patient DTM reconstruction, the proposed methods effectively suppressed both the detector boundary artifact and glaring artifact, which strongly degraded the visibility of the breast structures in the boundary areas where the PV images were severely truncated. The local breast tissue details were essentially recovered.

Conclusion:

Both the detector boundary truncation artifact due to the limited detector size and the glaring artifact due to the limitation of the imaged volume have been substantially reduced and the overall image quality of the truncated boundary regions is significantly improved. The recovered breast tissue details provide useful information in breast cancer detection and diagnosis.

(D) Investigation of the impact of DTM system and imaging condition parameters on the reconstructed image quality

The development of DTM system and the selection of optimal imaging conditions are still in the early stage. The image quality depends on a lot of factors including hardware, system design, imaging conditions, reconstruction algorithms and many other parameters. It is therefore of practical importance to investigate the impact of DTM system design on image quality. The results will provide insight and useful information for trade-offs between system design and optimizing image conditions.

Method:

We used both breast phantom and developed computer simulation models to conduct this study. The breast phantoms are similar to those used in the abovementioned studies. For computer simulation, the same GE prototype DTM system was modeled and forward projection images of software phantom were generated. Ultra-high resolution of isotropic voxel lattice was used.

We have investigated a number of different imaging conditions, including different distributions (or sampling) of PV images for a fixed total dose, different combinations of number of PVs, total angular range and angular increment, on the reconstructed image quality. Among many image quality measures, we were particularly interested in Z-axis resolution (depth resolution). The Z-axis resolution represents the ability of the DTM system to distinguish adjacent objects along the depth direction and therefore is one of the most important advantages provided by DTM to separate overlapping breast tissues occurred in conventional mammograms. With the ultra-high resolution of the simulation model, a “point” like object can be used to evaluate Z-axis resolution at specific location. To quantitatively evaluate the Z-axis resolution for different DTM imaging conditions, the vertical line profile along the Z-axis and through the point object center was extracted from the reconstructed volume. The line profile was then normalized to 1 at the maximum value. The full-width-at-half-maximum (FWHM) of the normalized line intensity profile was used to evaluate the Z-axis resolution. For a

given DTM imaging condition, we also compared the Z-axis resolution of SART method to BP method.

Result:

Preliminary phantom and computer simulation studies demonstrated that: (1) the larger the DTM angular range, the better the CNR and ASF of simulated masses; while the narrow angular range gave sharper in-plane edge for high-density objects. (2) image sharpness and contrast decreased with decreasing numbers of PVs used in the reconstruction. The interplane artifacts increased with decreasing angular range of the PVs. (3) The Z-axis resolution is relatively independent of depth within a typical breast thickness range (i.e. a 5-cm-thick volume) and the number of projection views within a fixed angular range, but strongly affected by tomo-angle such that the depth resolution improves with increasing total tomosynthesis angle. The SART method can provide better Z-axis resolution than the BP method.

Conclusion:

DTM system design and imaging condition parameters have significant impact on reconstruction image quality. Our investigation has revealed some important tradeoff between different parameter combinations. Further work is underway to continue the studies of these relationships.

Key Research Accomplishments

- Develop breast phantom and a variety of figures of merit for quantitative evaluation of image quality and artifact reduction ------ (Task 1 (a))

- Implement multiple three-dimensional limited-angle cone-beam tomographic algorithms for DTM reconstruction, including Shift-and-Add (SAA) method, back-projection (BP) method, FDK filtered back-projection method, algebraic reconstruction techniques (ART, SART, SIRT), and statistical methods (maximum likelihood method with gradient algorithm and maximum likelihood method with convex method) ------ (Task 1(b))

- Quantitatively evaluate and compare representative DTM algorithm, including BP, SART and ML-Convex method; and investigate the impact of a number of factors, including initialization, number of iterations, relaxation parameter and PV image accessing strategy, on the reconstructed image quality of SART ------ (Task 1 (c) and (d))

- Develop a 2D breast boundary segmentation method on PV images and a 3D surface-generating method to estimate breast shape information ------ (Task 2 (a), (b) and (c))

- Incorporate both 2D and 3D breast shape information in iterative DTM reconstruction algorithm to achieve efficient implementation and reduce boundary artifacts ------ (Task 2 (d) and (e))

- Develop and evaluate artifact reduction methods with both breast phantom study and patient cases for DTM image artifacts from multiple sources, including boundary artifacts, truncation artifacts, glaring artifacts and ghost shadow artifacts of high-density objects ------ (Task 2 (e))

Reportable Outcomes

With the support by USAMRMC, we have successfully conducted studies in digital tomosynthesis mammography in this project year. We have published the results in peer-reviewed journal and presented the work in international conferences, as listed in the following.

<u>Peer-Reviewed Journal Articles:</u>

1. Y. Zhang, H.-P. Chan, B. Sahiner, Y.-T. Wu, C. Zhou, J. Ge, J. Wei, L. M. Hadjiiski, "Application of boundary detection information in breast tomosynthesis reconstruction", <u>Medical Physics</u>, 34(9), 3603-3613, 2007.

<u>Conference Proceedings:</u>

1. Y. Zhang, H.-P. Chan, Y.-T. Wu, B. Sahiner, C. Zhou, J. Wei, J. Ge, L. M. Hadjiiski, J. Shi, "Truncation artifact and boundary artifact reduction in breast tomosynthesis reconstruction", Proc SPIE 6913; 2008: 69132Y1-69132Y9.

2. J. Wei, H.-P. Chan, Y. Zhang, B. Sahiner, C. Zhou, J. Ge, Y.-T. Wu, L. M. Hadjiiski, "Classification of breast masses from normal tissues on digital tomosynthesis mammography", Proc SPIE 6915; 2008: 6915081-6915086.

3. J. Ge, H.-P. Chan, B. Sahiner, Y. Zhang, J. Wei, L. M. Hadjiiski, C. Zhou, Y.-T. Wu, J. Shi, "Digital tomosynthesis mammography: Improvement of artifact reduction method for high-attenuation objects on reconstructed slices", Proc SPIE 6913; 2008: 69134O1-69134O6.

4. H.-P. Chan, Y.-T. Wu, B. Sahiner, Y. Zhang, J. Wei, R. H. Moore, D. B. Kopans, M. A. Helvie, L. M. Hadjiiski, T. Way, "Digital tomosynthesis mammography: comparison of mass classification using 3D slices and 2D projection views", Proc SPIE 6915; 2008: 6915061-6915066.

5. Y. Zhang, H.-P. Chan, M. M. Goodsitt, A. Schmitz, J. W. Eberhard, B. E. H. Claus, "Investigation of different PV distributions in Digital Breast Tomosynthesis (DBT) Mammography", International Workshop on Digital Mammography (IWDM), Tucson, AZ, July 2008, (in press).

<u>Conference Abstracts and Presentations:</u>

1. H.-P. Chan, Y.-T. Wu, B. Sahiner, Y. Zhang, R. Moore, D. Kopans, L. M. Hadjiiski M. A. Helvie, "Digital Breast Tomosynthesis Mammography: Computerized Classification of Malignant and Benign Masses", Oral presentation at the 49th Annual Meeting of the American Association of Physicists in Medicine (AAPM), Minneapolis, MN. July 22-26, 2007.

2. Y. Zhang, H.-P. Chan, B. Sahiner, Y.-T. Wu, C. Zhou, J. Ge, J. Wei, L. M. Hadjiiski, "Breast tomosynthesis reconstruction with simultaneous algebraic reconstruction technique (SART): Truncation Artifact and Boundary Artifact Reduction", The 93rd Scientific Assembly and Annual Meeting of RSNA, Chicago, IL, 2007, RSNA Program Book, pp 316.

3. A. V. Nees, B. Sahiner, Y. Zhang, A. Joe, H.-P. Chan, P. Carson, "Digital Breast Tomosynthesis vs. Conventional Mammography: Early Experience with Comparison of Breast Mass Detection and Characterization", The 93rd Scientific Assembly and Annual Meeting of RSNA, Chicago, IL, 2007, RSNA Program Book, pp 704.

4. H.-P. Chan, Y.-T. Wu, B. Sahiner, Y. Zhang, R. H. Moore, D. B. Kopans, M. A. Helvie, L. M. Hadjiiski, "Analysis of Mass Characteristics on Digital Breast Tomosynthesis (DBT) Mammograms: Application to computer-aided diagnosis", The 93rd Scientific Assembly and Annual Meeting of RSNA, Chicago, IL, 2007, RSNA Program Book, pp 315.

5. M. A. Helvie, M. A. Roubidoux, L. M. Hadjiiski, Y. Zhang, P. L. Carson, H.-P. Chan, "Tomosynthesis Mammography versus Conventional Mammography: Comparison of Breast Masses Detection and Characterization", The 93rd Scientific Assembly and Annual Meeting of RSNA, Chicago, IL, 2007, RSNA Program Book, pp 381.

Conclusion

During the first year of the project, we have completed a number of studies in the development of advanced reconstruction algorithms for DTM. We have implemented and compared some representative reconstruction algorithms for limited-angle cone-beam tomographic problem in DTM. The SART method, a member of the family of algebraic reconstruction techniques, has been found effective in providing good image quality and being more efficient than statistical methods. A variety of reconstruction parameters, including initialization, number of iterations, relaxation parameter and PV accessing order, were investigated in an effort to optimize SART reconstruction. Multiple dedicated breast phantoms and image quality measures were developed during the study to facilitate qualitative and quantitative evaluations. An efficient algorithm was developed to reduce the computational time of iterative reconstruction method by incorporating breast shape information that is available from PV images and the DTM geometry. Artifact reduction methods have been developed to suppress DTM image artifacts from multiple sources, including breast boundary shadows, truncation of PV images and the limited size of the modeled imaged volume. The advanced SART method with all abovementioned components can provide a fast, consistent and satisfactory DTM reconstruction with improved image quality and minimized artifacts. In addition, we have investigated the relationship of DTM imaging condition parameters, particularly the distribution of PV images, to reconstruction image quality based on our developed advanced SART method. The study results contribute to the understanding of important tradeoffs between different DTM system design parameters.

In the coming year, we will investigate the scatter and beam hardening effect in DTM reconstruction. We will develop artifact reduction methods for these two problems and further improve DTM reconstruction image quality and the quantitative estimation of

x-ray attenuation properties of breast tissue. We will also continue our study in reduction of other important DTM image artifacts that will benefit the quantitative reconstruction of DTM imaging.

References

None

Appendices

Copies of the following publications are enclosed with this report.

Peer-Reviewed Journal Articles:

1. Y. Zhang, H.-P. Chan, B. Sahiner, Y.-T. Wu, C. Zhou, J. Ge, J. Wei, L. M. Hadjiiski, "Application of boundary detection information in breast tomosynthesis reconstruction", Medical Physics, 34(9), 3603-3613, 2007.

Conference Proceedings:

1. Y. Zhang, H.-P. Chan, Y.-T. Wu, B. Sahiner, C. Zhou, J. Wei, J. Ge, L. M. Hadjiiski, J. Shi, "Truncation artifact and boundary artifact reduction in breast tomosynthesis reconstruction", Proc SPIE 6913; 2008: 69132Y1-69132Y9.

2. J. Wei, H.-P. Chan, Y. Zhang, B. Sahiner, C. Zhou, J. Ge, Y.-T. Wu, L. M. Hadjiiski, "Classification of breast masses from normal tissues on digital tomosynthesis mammography", Proc SPIE 6915; 2008: 6915081-6915086.

3. J. Ge, H.-P. Chan, B. Sahiner, Y. Zhang, J. Wei, L. M. Hadjiiski, C. Zhou, Y.-T. Wu, J. Shi, "Digital tomosynthesis mammography: Improvement of artifact reduction method for high-attenuation objects on reconstructed slices", Proc SPIE 6913; 2008: 69134O1-69134O6.

4. H.-P. Chan, Y.-T. Wu, B. Sahiner, Y. Zhang, J. Wei, R. H. Moore, D. B. Kopans, M. A. Helvie, L. M. Hadjiiski, T. Way, "Digital tomosynthesis mammography: comparison of mass classification using 3D slices and 2D projection views", Proc SPIE 6915; 2008: 6915061-6915066.

5. Y. Zhang, H.-P. Chan, M. M. Goodsitt, A. Schmitz, J. W. Eberhard, B. E. H. Claus, "Investigation of different PV distributions in Digital Breast Tomosynthesis (DBT) Mammography", International Workshop on Digital Mammography (IWDM), Tucson, AZ, July 2008, (in press).

Application of boundary detection information in breast tomosynthesis reconstruction

Yiheng Zhang,[a)] Heang-Ping Chan, Berkman Sahiner, Yi-Ta Wu, Chuan Zhou, Jun Ge, Jun Wei, and Lubomir M. Hadjiiski
Department of Radiology, University of Michigan, Ann Arbor, Michigan 48109-0904

(Received 6 February 2007; revised 27 June 2007; accepted for publication 28 June 2007; published 22 August 2007)

Digital tomosynthesis mammography (DTM) is one of the most promising techniques that can potentially improve early detection of breast cancers. DTM can provide three-dimensional (3D) structural information by reconstructing the whole imaged volume from a sequence of projection-view (PV) mammograms that are acquired at a small number of projection angles over a limited angular range. Our previous study showed that simultaneous algebraic reconstruction technique (SART) can produce satisfactory tomosynthesized image quality compared to maximum likelihood-type algorithms. To improve the efficiency of DTM reconstruction and address the problem of boundary artifacts, we have developed methods to incorporate both two-dimensional (2D) and 3D breast boundary information within the SART reconstruction algorithm in this study. A second generation GE prototype tomosynthesis mammography system with a stationary digital detector was used for PV image acquisition from 21 angles in 3° increments over a ±30° angular range. The 2D breast boundary curves on all PV images were obtained by automated segmentation and were used to restrict the SART reconstruction to be performed only within the breast volume. The computation time of SART reconstruction was reduced by 76.3% and 69.9% for cranio-caudal and mediolateral oblique views, respectively, for the chosen example. In addition, a 3D conical trimming method was developed in which the 2D breast boundary curves from all PVs were back projected to generate the 3D breast surface. This 3D surface was then used to eliminate the multiple breast shadows outside the breast volume due to reconstruction by setting these voxels to a constant background value. Our study demonstrates that, by using the 2D and 3D breast boundary information, all breast boundary and most detector boundary artifacts can be effectively removed on all tomosynthesized slices.
[DOI: 10.1118/1.2761968]

Key words: digital tomosynthesis mammography (DTM), image reconstruction, simultaneous algebraic reconstruction technique (SART), breast boundary detection, boundary artifact reduction

I. INTRODUCTION

Currently mammography is the only proven method used for breast cancer screening. However, a major limitation of mammography is that the projection images, recorded on a screen-film system (conventional mammography) or by a digital detector (digital mammography), only contain two-dimensional (2D) projection of three-dimensional (3D) anatomical structures. As a result, the sensitivity of breast cancer detection is adversely affected by the camouflaging of cancerous lesions by dense breast tissues.

Digital tomosynthesis mammography (DTM) is one of the most promising techniques that can potentially improve early detection of breast cancers.[1–5] DTM can provide 3D structural information by reconstructing the whole imaged volume from a sequence of projection-view (PV) mammograms that are acquired at a small number of projection angles over a limited angular range. The total radiation dose is set to be comparable to that used in regular screening mammography. It has been demonstrated[6–8] that DTM can reduce the camouflaging effect of the overlapping fibroglandular breast tissue, thus improving the conspicuity of subtle lesions. Several prototype DTM systems have been developed based on digital mammography systems[5,9,10] and preliminary pilot clinical trials are being conducted to evaluate the utility of DTM.[11–13]

The reconstruction of the 3D volume of the compressed breast from a sequence of 2D projection images in DTM represents a limited-angle cone-beam tomographic problem. Current reconstruction methods for such a problem include

- Back-projection-type algorithms, including the shift-and-add method used in the original tomosynthesis[1,14] and multiple projection method;[15]
- Fourier-transform based algorithms, including the filtered back-projection (FBP) method[9,16,17] and other transfer function methods, such as inversion filtering[10,18,19] and matrix inversion tomosynthesis (MITS);[20–22]
- Algebraic reconstruction techniques (ARTs), including the original ART[16,23] and simultaneous ART (SART);[24,25]
- Statistical reconstruction algorithms, including maximum likelihood (ML) method with convex algorithm.[26,27]

Due to the limited angular range employed in DTM acquisition, only incomplete projection information of the imaged breast is available which results in intra- and inter- slice artifacts. The inter-slice artifacts come from the superposition of out-of-plane features on the in-focus plane which cannot be removed by DTM reconstruction alone. Many artifact reduction algorithms have been investigated, especially those to address artifacts of high attenuation objects, including deblurring techniques,[28–31] order statistics operator,[32,33] and voting strategies,[34] and these methods have been incorporated into various reconstruction methods.

A review of tomosynthesis reconstruction techniques can be found in Dobbins and Godfrey.[20] In our previous work,[25] we have investigated three representative methods for DTM reconstruction based on breast phantom study and a second generation GE prototype DTM system: the back-projection method, the SART and the maximum likelihood method with the convex algorithm (ML-Convex). Our comparative study suggested that both SART and ML-Convex methods can achieve good-quality reconstruction and the SART method can provide comparable tomosynthesized image quality to those of ML-Convex method but with fewer number of iterations.

Two important aspects should be considered in breast tomosynthesis reconstruction. First, the demand on high spatial resolution results in a very high dimensionality of the inverse problem and prohibitive computational burden. It is therefore important to investigate methods to avoid unnecessary computation. Some parallel computation method[27] and hardware acceleration techniques[35] have been recently developed to improve the speed of DTM reconstruction. However, these methods are usually dedicated to specific reconstruction algorithms and the improvement depends on the algorithm under consideration. Since these dedicated software or hardware cannot be easily developed for every reconstruction technique, it is of practical importance to design methods to improve the computational efficiency, especially at the stage when the reconstruction algorithm is still being developed. Second, the DTM reconstruction is a severely underdetermined and ill-posed inverse problem due to the limited number of projections and the limited angular range which only provides incomplete projection information of the imaged breast. As a result, tomosynthesis reconstruction generally contains strong artifacts. These artifacts are represented as repeating ghosts along the x-ray path directions on all tomosynthesized slices with reduced intensity. These artifacts also appear at the breast boundary in which the pixel intensity changes abruptly from breast tissue to air on PV images. The breast boundary artifacts, although easily distinguishable from breast anatomical features, could be distracting for radiologists' reading. Furthermore, these artifacts could negatively affect computerized processing of DTM images, e.g., computer-aided detection of mass lesions by using DTM reconstruction images.[25,36]

In this work, we developed a 3D conical trimming method based on back projection of the breast boundaries detected on the 2D PV images to generate the 3D breast surface and extract the breast volume. We investigated the application of

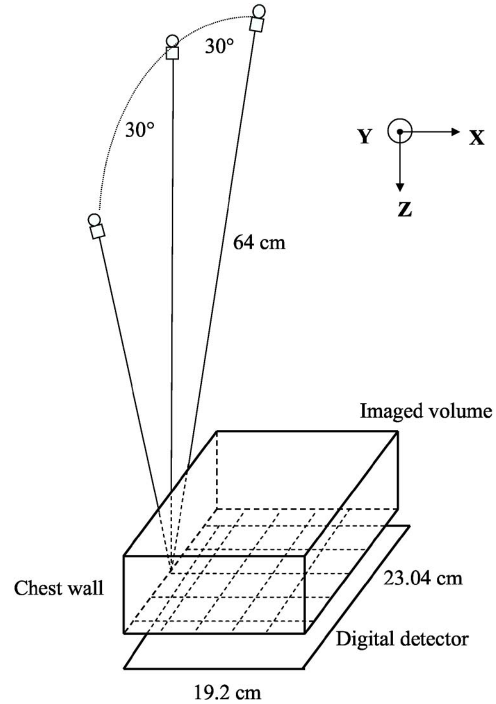

FIG. 1. Geometry of the second generation GE prototype digital tomosynthesis mammography system used in this study.

the 2D and 3D breast boundary information to DTM reconstruction in an effort to reduce computational burden and to suppress boundary artifacts. With 2D breast boundary information on PV images, the reconstruction algorithm will only consider the x-rays that intercept the breast volume. This will eliminate unnecessary computation outside the breast while keeping all useful information for reconstruction. Using patient DTM images, we demonstrate that the 2D and 3D information can be used to effectively remove two boundary artifacts: breast boundary artifacts and detector boundary artifacts, from the reconstructed DTM slices.

II. MATERIALS AND METHODS

II.A. Breast tomosynthesis system

The imaging geometry of the second generation GE prototype digital tomosynthesis system for breast imaging research is shown in Fig. 1. The DTM system has a CsI phosphor/a:Si active matrix flat panel digital detector with dimensions of 19.20 cm $\times$ 23.04 cm and a pixel size of 0.1 mm $\times$ 0.1 mm. The digital detector is stationary during image acquisition. The DTM system acquires PV images at 21 different angles over a ±30° angular range by automatically rotating the x-ray tube in 3° increments. The distance from the x-ray focal spot to the center of rotation is 64 cm and the plane along which the x-ray source rotates is perpendicular to the detector surface at the chest wall edge. The focal-spot-to-detector distance is 66 cm. The image acquisition process takes less than 8 s.

In our reconstruction algorithm, we define the "imaged volume" as a rectangular box having the same area as the

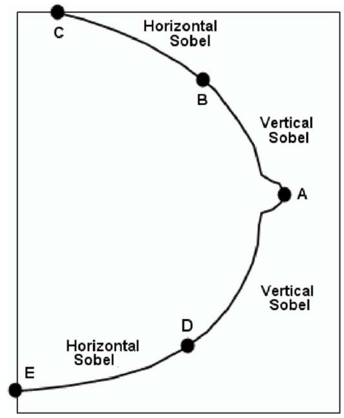

FIG. 2. The use of vertical and horizontal Sobel filtering in the breast boundary tracking procedure.

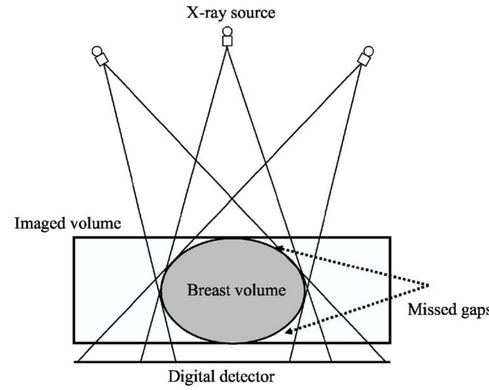

FIG. 3. Estimation of the 3D breast surface from 2D breast boundary curves by 3D conical trimming of the volume outside the breast. Dashed arrows indicate the potential missed gaps for which the breast surface cannot be recovered.

detector, and the same thickness as that of the compressed breast measured by the DTM system, as shown in Fig. 1. This imaged volume is subdivided into an array of voxels, of which the X and Y dimensions are chosen to be the same as the pixel size of the detector ($0.1\ \text{mm} \times 0.1\ \text{mm}$) while the Z dimension (the slice thickness) is chosen to be 1 mm in this study.

As described in our previous paper,[25] for the forward projection model, we have developed an algorithm to calculate the path length of a primary x-ray intersecting each voxel within the imaged volume lattice, similar to Siddon's algorithm.[37] Logarithmic transformation is applied to the raw pixel intensities of the detected image before reconstruction in the SART method. We assume a monoenergetic x-ray source and ignore the effects of scattering and beam hardening in this study, similar to the approach by Wu *et al.*[2,38]

II.B. Detection of 2D breast boundary and generation of 3D breast surface

The 2D breast boundary on a PV image is segmented by a breast boundary detection program developed in our laboratory[39,40] and adapted to suit DTM application. There are two main steps in the algorithm. In the first step, the initial breast boundary is obtained by applying Otsu's thresholding method[41] to the histogram of the input image. The initial boundary is only a rough estimate of the boundary location so that gray level thresholding is sufficient. In the second step, a breast boundary tracking procedure is performed, using the initial boundary as a guide, by extracting gradient information from horizontal and vertical Sobel filtering. The application of the Sobel filters is illustrated in Fig. 2. The right-most pixel of the initial boundary is first determined, as indicated by point A in Fig. 2. Although this point coincides with the nipple location in this figure, it can be any point along the boundary. The tracking procedure starts from point A and moves upward and downward, respectively, to determine the final breast boundary. The vertical Sobel filter is used to enhance the edges in the ranges between A and B and between A and D, and the horizontal Sobel filter is used in the ranges between B and C and between D and E. The selection of either the vertical or horizontal Sobel filter is determined based on the slope of the tangent to the current boundary tracking position. From our experience, this relatively simple boundary detection method is reliable for the DTM PV images we have processed so far. However, the focus of this work is not on the development of image segmentation methods. Our breast surface reconstruction algorithm described below does not depend on the boundary detection method so that any satisfactory breast boundary curves for DTM PV images obtained with our method or other segmentation techniques can be used.

With the detected 2D breast boundary curves on all PV images, we can generate a 3D breast surface within the imaged volume to enclose the compressed breast while excluding the exterior air space. In principle, there exists a unique convex hull inside the 3D imaged volume for the DTM system of which the projections at different angles precisely correspond to the breast shadow on each PV image. To recover this convex hull, we implement a "3D conical trimming" process. This process is schematically depicted in Fig. 3 where only three x-ray source positions are drawn for illustration. Specifically, for a given PV image, the breast boundary curve is back projected into the imaged volume and all "air volume" outside the generalized cone surface formed by the x-ray source and the breast boundary is trimmed off. This process will repeat for all PV images. As the x-ray source moves from one to the next position, the back-projected breast surface will trim off more air-volume in addition to the preceding ones. After all PV breast boundary curves have been used exactly once, the surface of the remaining volume becomes the desired convex hull and its projection with respect to each x-ray source position corresponds to exactly the breast shadow. The convex hull combined with the top and bottom surfaces of the breast delineated by the compression paddle and the breast support plate define an enclosed breast volume.

Note that for any x-ray source position, some parts of the imaged volume will not be included in the cone-beam ray path, and at larger projection angles, some parts of the projected image will be cut off due to the limited detector size.

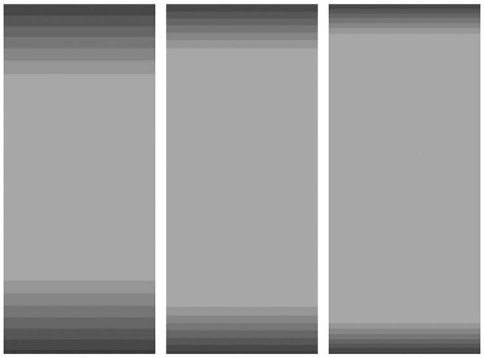

FIG. 4. PV-count maps of three selected depths: (a) 5.0 cm, (b) 2.5 cm, and (c) 1.0 cm above the breast support plate. The darker pixel intensity represents a fewer number of effective PVs. For all three slices, the top-most area contains only eight PVs and the bottom-most area contains only seven PVs. This number gradually increases to 21 from both ends to the middle region.

This problem is accentuated in a DTM system with a stationary detector. For different x-ray source positions, the unexposed parts of the imaged volume change. The overall effect is that some middle part of the imaged volume is completely inside the x-ray path at all times, i.e., exposed by all 21 PVs; and for other parts, it is exposed by only a subset of the 21 PVs. Figure 4 shows examples of the PV-count maps, in which the intensity of a given pixel is proportional to the number of PVs contributing radiation to this pixel. The PV-count maps of three tomosynthesized slices at depths, 5.0, 2.5, and 1.0 cm, above the breast support plate, are shown. It can be seen that all PVs contribute to the middle region of each tomosynthesized slice, and this region grows larger as the distance from the support plate decreases. The number of steps on each side is determined by the imaging geometry of the DTM system, and is equal to the number of PVs of which the x-ray field boundary intersects the imaged volume on that side. Furthermore, for any tomosynthesized slice, the closer the region is to the imaged volume boundary, the fewer the number of PVs will expose the region, as apparent from the DTM geometry. In this specific example that we acquired with our GE prototype DTM system, only eight PVs can expose the uppermost while seven for the lowest boundary area on all tomosynthesized slices. Therefore 13 and 14 steps, respectively, can be seen on the upper and lower sides of the PV-count map. The unequal PV-count numbers on the upper and lower boundary areas may be attributed to the slightly asymmetric angular positions of the x-ray source relative to the central location.

According to the 3D conical trimming process, for the fully exposed parts of the imaged volume (in terms of PVs), the 3D breast surface tangential to the x rays can be generated by the intersection of all back-projected 2D breast boundary curves. Thus, a voxel can be considered to be inside the breast volume if and only if its projection is within the breast boundary in all PVs. In contrast, in any partially exposed parts of the imaged volume, a voxel is considered to be inside the breast volume as long as its projection is within the breast boundary of any PV. This process ensures that any potential breast volume which may be contained only in some of the PV images due to the detector cutoff will be included. All voxels in the air volume above and below the breast volume will be excluded by the breast boundaries defined by the compression paddle and the breast support plate.

II.C. Simultaneous algebraic reconstruction technique (SART) and boundary artifacts

SART method[24,42] is an iterative reconstruction technique. It was proposed as a refinement of the original ART.[16,43,44] In SART method, an update of the 3D distribution of the attenuation properties of the imaged volume is performed based on each PV. The calculated current projection will be compared to the actual detection data and the difference will be back projected and added to the imaged volume distribution. The updating is performed after all rays in one PV have been processed, resulting in a "block-iterative" strategy. In contrast, ART method updates the distribution based on a ray-by-ray manner. The number of updates in one complete iteration of SART is equal to the number of PVs.

Let the whole image volume be subdivided into J voxels, and the linear attenuation coefficient for the jth voxel be denoted by x_j, $1 \le j \le J$; the digital area detector contains I elements, and the ith ray, $1 \le i \le I$, is defined as a line segment starting from the point x-ray source location to the center of the ith detector element. The number of rays is equal to the number of detector elements assuming one ray is traced for each element. The path length of the ith ray going through the jth voxel in the nth x-ray tube location (projection view) is denoted by $a_{ij,n}$, resulting in a matrix-vector form of the projection model as

$$\mathbf{A}_n \mathbf{x} = \mathbf{y}_n, \tag{1}$$

where $\mathbf{A}_n$ is the projection matrix for the nth PV with $a_{ij,n}$ as its (i,j)th element; $\mathbf{y}_n$ is the corresponding vector of the projection data, which can be derived from the pixel values of the detected image, $1 \le n \le N$, where N is the total number of PVs. The ith projection value, $y_{i,n}$, is proportional to the logarithmic transform of the ratio of the incident intensity $(I_{o,n})$ and the transmitted intensity $(I_{i,n})$ of the ith ray

$$y_{i,n} = k \ln \frac{I_{o,n}}{I_{i,n}}. \tag{2}$$

We stack the projection model in Eq. (1) for all PVs together as

$$\begin{bmatrix} \mathbf{A}_1 \\ \vdots \\ \mathbf{A}_N \end{bmatrix} \mathbf{x} = \begin{bmatrix} \mathbf{y}_1 \\ \vdots \\ \mathbf{y}_N \end{bmatrix} \to \mathbf{A}\mathbf{x} = \mathbf{y}. \tag{3}$$

With the linear system model in Eq. (3), the SART method can be formulated in a matrix-vector form as

$$\mathbf{x}^n = \mathbf{x}^{n-1} + \lambda \cdot \mathbf{M}_n \mathbf{A}_n^T \mathbf{W}_n (\mathbf{y}_n - \mathbf{A}_n \mathbf{x}^{n-1}), \tag{4}$$

where $\mathbf{M}_n \in R^{J \times J}$ and $\mathbf{W}_n \in R^{I \times I}$ are diagonal matrices containing diagonal elements as $[\mathbf{M}_n]_{jj} = (\Sigma_{i=1}^{I} a_{ij,n})^{-1}$ and $[\mathbf{W}_n]_{ii} = (\Sigma_{j=1}^{J} a_{ij,n})^{-1}$, respectively. One can see that $\mathbf{M}_n$ and

$\mathbf{W}_n$ contain inverse "column sum" and "row sum" of the projection matrix $\mathbf{A}_n$ that correspond to the total path length of all x-rays through one imaged voxel and the total path length of one x-ray through the entire imaged volume, respectively. The updating strategy of SART is easy to understand based on Eq. (4) as follows: the calculated projection $\mathbf{A}_n\mathbf{x}^{n-1}$ is compared to the current PV data $\mathbf{y}_n$; the difference $(\mathbf{y}_n-\mathbf{A}_n\mathbf{x}^{n-1})$ is normalized by the total path length of each x-ray $\mathbf{W}_n$, yielding the estimated weighted average difference in the linear attenuation coefficient of the voxels along the ray. This average difference is back projected to the imaged volume by $\mathbf{A}_n^T$, and then for any given voxel, the differences are further normalized by the total path lengths of all rays traveling through this voxel by $\mathbf{M}_n$. The voxel is updated as the sum of the current estimation $\mathbf{x}^{n-1}$ and the weighted average difference scaled by a relaxation parameter λ. The updating operation starts from an initial distribution $\mathbf{x}^0$ and is repeated for all PV images using the corresponding projection matrices. One complete iteration is defined as the process that all PV images have been sequentially used exactly once. In our previous work,[25] we experimentally demonstrated that SART method can provide satisfactory tomosynthesized image quality with one complete iteration using all PV images and $\lambda=0.5$.

In this work, we focus on two types of boundary artifacts: one from the breast boundary and the other from the detector boundary. Breast boundary artifacts are caused by the large difference in the pixel intensities in the two areas inside and outside the 2D breast boundary, corresponding to projection of overlapping breast tissues and air volume, respectively. Due to the uncertainty in the true 3D location of any feature within the imaged volume based on a limited number of PV images over a limited acquisition angular range, when back projected by DTM reconstruction methods, these boundaries in the PVs will result in repeating ghost artifacts of similar breast shape but reduced intensity on all tomosynthesized image slices.

Detector boundary artifacts are caused by the DTM system geometry in which a stationary finite-size detector acquires PV images of the breast from moving x-ray source positions, as discussed in Sec. II B. In every PV position, a part of the imaged volume is not exposed by the cone-beam ray path and recorded by the detector, as shown in Fig. 5(a). The unexposed part of the imaged volume varies as the x-ray source moves. When we reconstruct the imaged volume using the SART method,[25] the voxel values will be updated iteratively by processing each individual PV image. For a given PV, only the part of the imaged volume within the current field of view will be updated. Since the voxels within the PV image boundary (i.e., the detector boundary) will be changed whereas the neighboring voxels outside will maintain their previous values, it will cause a discontinuity in the voxel values across the image boundary. Similar situation occurs when the breast image exceeds the detector area and the real breast boundary is outside the detector boundary, as schematically shown in Fig. 5(b). This situation occurs most frequently on the PV images associated with large projection

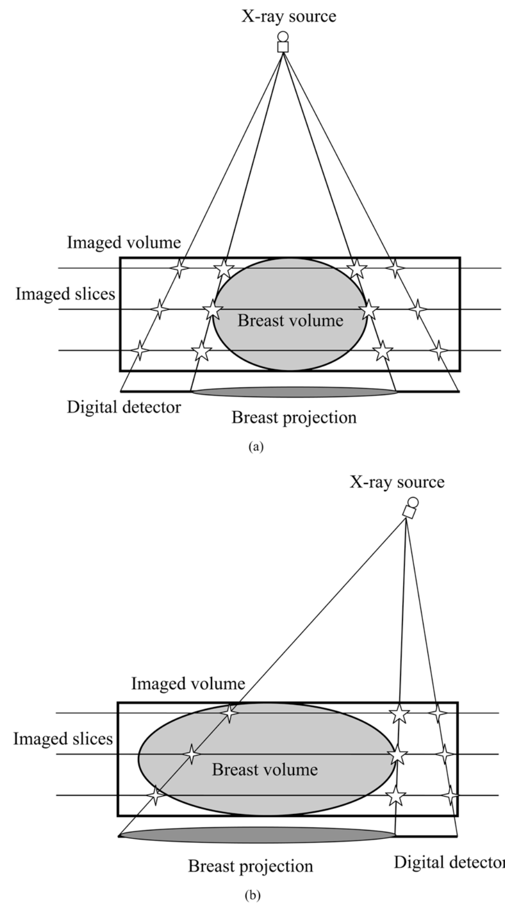

FIG. 5. Breast boundary artifacts (indicated by open stars) and detector boundary artifacts (indicated by open crosses) appear on all tomosythesized slices along the x-ray path for one x-ray source position. The imaged volume is defined as the volume enclosed by the rectangular box while the breast volume is that enclosed by the ellipse. This example shows the situations (a) that the breast boundary is completely contained within the detector boundary; (b) that one side of the breast boundary is cut off by the detector boundary due to both the large breast size and the wide projection angle.

angles, in the cases of very large breast sizes, or at the top part of the pectoral muscle on most MLO views.

As an example, Fig. 6(a) shows a patient CC-view DTM slice reconstructed by the SART method with one iteration. The breast boundary artifacts were clearly seen as repeated breast-shaped shadows and the detector boundary artifacts as multiple horizontal lines in both the top and the bottom areas.

The breast boundary artifacts generally will be enhanced, rather than reduced, by the SART method as the number of iteration increases until a convergent solution is reached. This is because the SART method, similar to other iterative reconstruction algorithms, acts like an unsharp-masking (bandpass) filter in updating the imaged volume and thus favors edge enhancement. The convergent solution, however, will generally be very noisy due to the severe ill-posed nature of the inverse problem.

For detector boundary artifacts, they may be enhanced or reduced in the process of approaching the convergent solu-

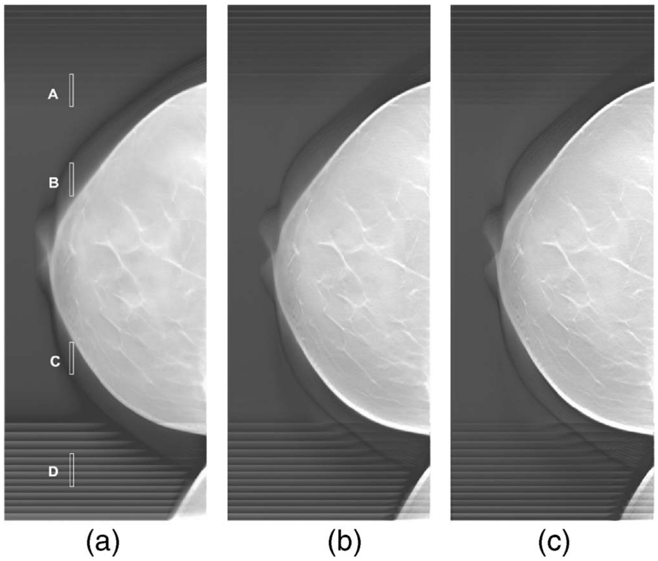

FIG. 6. One selected tomosynthesized slice obtained by SART reconstruction method with (a) one, (b) two, and (c) three iterations, without using any breast boundary information. The breast boundary artifacts were clearly observed as repeated breast-shaped shadows while the detector boundary artifacts as multiple horizontal lines in both the top and the bottom areas. The same window level and window width were used for display of the images. The artifacts did not diminish as the number of iterations increased. Open rectangles in (a) indicate the regions of interest for which the line profiles are compared in Fig. 7.

tion, depending on the access order of the PVs in the iterative reconstruction process. To demonstrate these effects, we applied the SART reconstruction method to the patient CC-view DTM up to three iterations, and presented the result of the same tomosynthesized slice in Figs. 6(b) and 6(c), respectively. A constant relaxation parameter of 0.5 was used for all three SART iterations. Four regions of interest, depicted by open rectangles in Fig. 6(a), were selected for comparison. Regions A and D are located in the detector boundary artifact area while regions B and C in the breast boundary artifact area. The line profiles in these four regions are shown in Fig. 7. The enhancement of both types of boundary artifacts by SART iterations can be observed clearly in regions A, B and C. In region D, the detector boundary artifacts were more prominent than those in region A at the upper part. This difference can be attributed to the access order of the PV images employed in SART reconstruction of this example, sequentially from that with the x-ray source at the top side to the bottom side.[45] The upper part of the imaged volume were covered completely and thus updated uniformly by the first eight PVs at the beginning of the iteration. The voxels of the entire region therefore attained reasonable values before the subsequent PVs that partially covered the upper part of the imaged volume started to generate the detector boundary artifacts. On the contrary, the artifacts at the lower part were generated starting from the first PV. The large difference between the initialization constant values outside the PV image and the updated voxel values within the PV image resulted in large discontinuity in the voxel values across the detector boundary. Although the

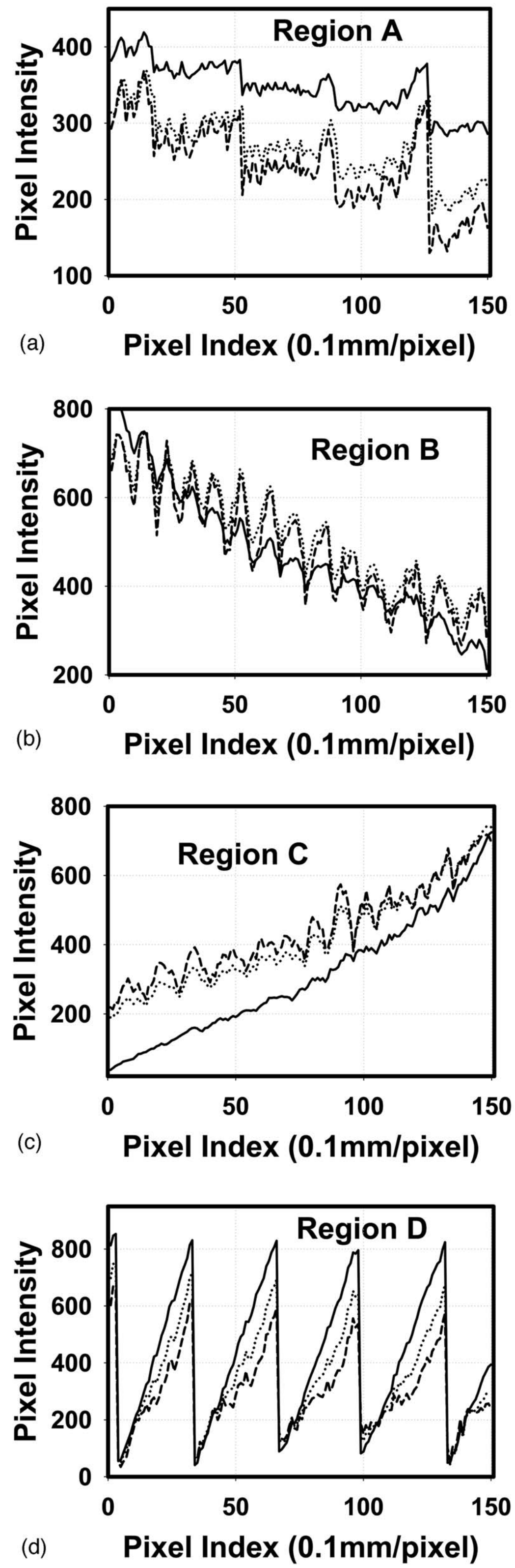

FIG. 7. comparison of line profiles extracted from selected detector boundary artifact areas (regions A and D) and breast boundary artifact areas (regions B and C) of SART results with one (solid line), two (dotted line) and three iterations (dashed line). The locations of these selected regions are indicated by open rectangle in Fig. 6(a). Pixel index always starts from the end that is close to the bottom part of the tomosynthesized slice.

subsequent iterations still enhanced the edges, their dominant effect was to bring the average voxel values to the level of those of air attenuation. The overall result was the apparent reduction of edge artifacts with further iterations in region D, opposite to those observed in the other regions.

To verify these, we continued the SART reconstruction up to ten iterations and observed that the iteration appeared to have reached a convergent solution for this DTM case (results not shown here). The reconstructed background was close to the local background level and the boundary artifacts became more symmetric in the upper and lower parts of the slices. The line profiles of regions A and D in the convergent result exhibited similar detector boundary artifacts which did not vanish with further iterations. Note that, because the large number of iterations causes over enhancement of the breast structures and excessive computation time, the reconstruction will generally terminate long before it reaches the convergent solution. We have found in our previous study[25] that good-quality patient DTMs can be achieved after only one iteration with SART.

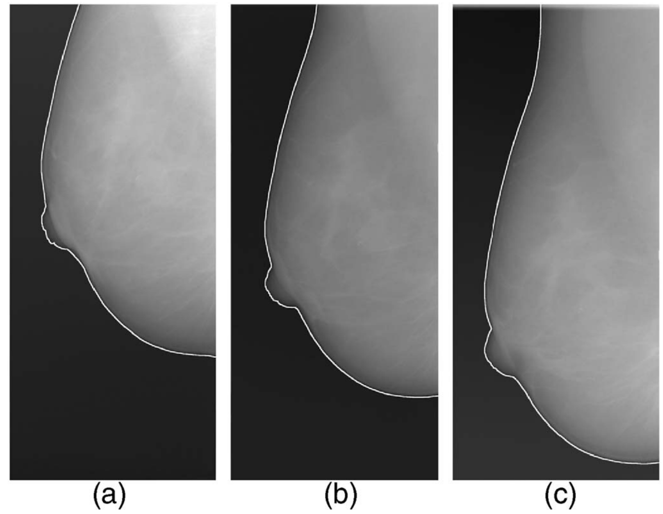

FIG. 8. Projection view images of a DTM in MLO view: (a) PV at −30°, (b) PV at 0°, and (c) PV at +30°. The x-ray source moved in the vertical direction relative to the images shown. The detected breast boundary was indicated by the white solid line on each PV image

II.D. Application of the 2D and 3D breast boundary information to SART reconstruction

We evaluated the application of breast boundary information to DTM reconstruction in two ways with the SART method. First, when we update the imaged volume in the iterative process, the re-projection and the back-projection of the difference between the calculated data and the measured data will only be performed along those "valid" rays within the 2D breast area. We will not use any other rays and thus the voxels in the imaged volume associated with these "invalid" rays are not updated and stay at the current values. Second, after one complete SART iteration has been performed, we use the 3D breast surface to mask the resulting volume and set the values of all voxels outside the breast surface to that of air.

In terms of Eq. (4), the use of the 2D breast curves and the 3D breast surface can each be expressed as a linear operator in matrix form, denoted by diagonal matrices $\mathbf{P}_n \in R^{I\times I}$ and $\mathbf{Q} \in R^{J\times J}$, respectively, where the diagonal element of $\mathbf{P}_n$ is 1 if the corresponding detector element is marked as breast area in the nth PV, and 0 as air area; similarly, the diagonal element of $\mathbf{Q}$ is 1 if the corresponding voxel is marked as breast volume, and 0 as air volume. By using these linear operators, the SART method can be modified as follows:

$$\mathbf{x}^n = \mathbf{x}^{n-1} + \lambda \cdot \mathbf{M}_n \mathbf{A}_n^T \mathbf{W}_n \mathbf{P}_n (\mathbf{y}_n - \mathbf{A}_n \mathbf{x}^{n-1})$$
$$\mathbf{x}^N = \mathbf{Q}\mathbf{x}^N. \tag{5}$$

Note the operator $\mathbf{Q}$ is applied after one SART iteration is completed.

Our proposed method reduces the computational effort by eliminating the processing of all rays outside the breast region on each individual PV. Thus the improved efficiency ratio can be defined as the summation of the background areas outside the detected breast boundary on all PV images divided by the product of the detector area and the number of PVs.

III. RESULTS

The proposed method for artifact reduction has been evaluated by using patient PV images acquired with the second generation GE prototype DTM system. Institutional Review Board approval and informed consent were obtained for collection of the patient cases. DTM images were acquired in two views: a cranio-caudal (CC) view and a mediolateral oblique (MLO) view. In the rest of the paper, only image results of MLO view were shown without loss of generality. CC view results were similar to those of MLO views on the side without the pectoral muscle. The No. 1, No. 11 and No. 21 raw PV images of MLO view, corresponding to the projection angles −30°, 0°, +30°, are shown in Fig. 8. The detected breast boundaries were indicated by solid white lines. The x-ray source moved in the vertical direction relative to the images shown. Figure 9 shows the generated 3D

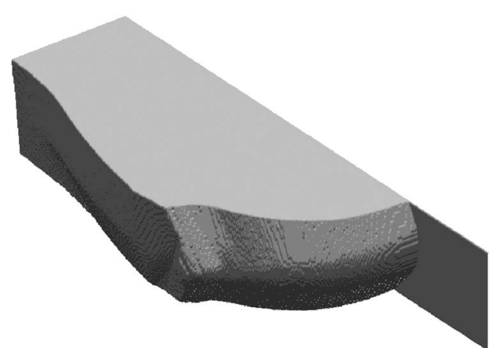

FIG. 9. The 3D breast surface generated from 2D breast boundary curves for MLO view by using the 3D conical trimming method.

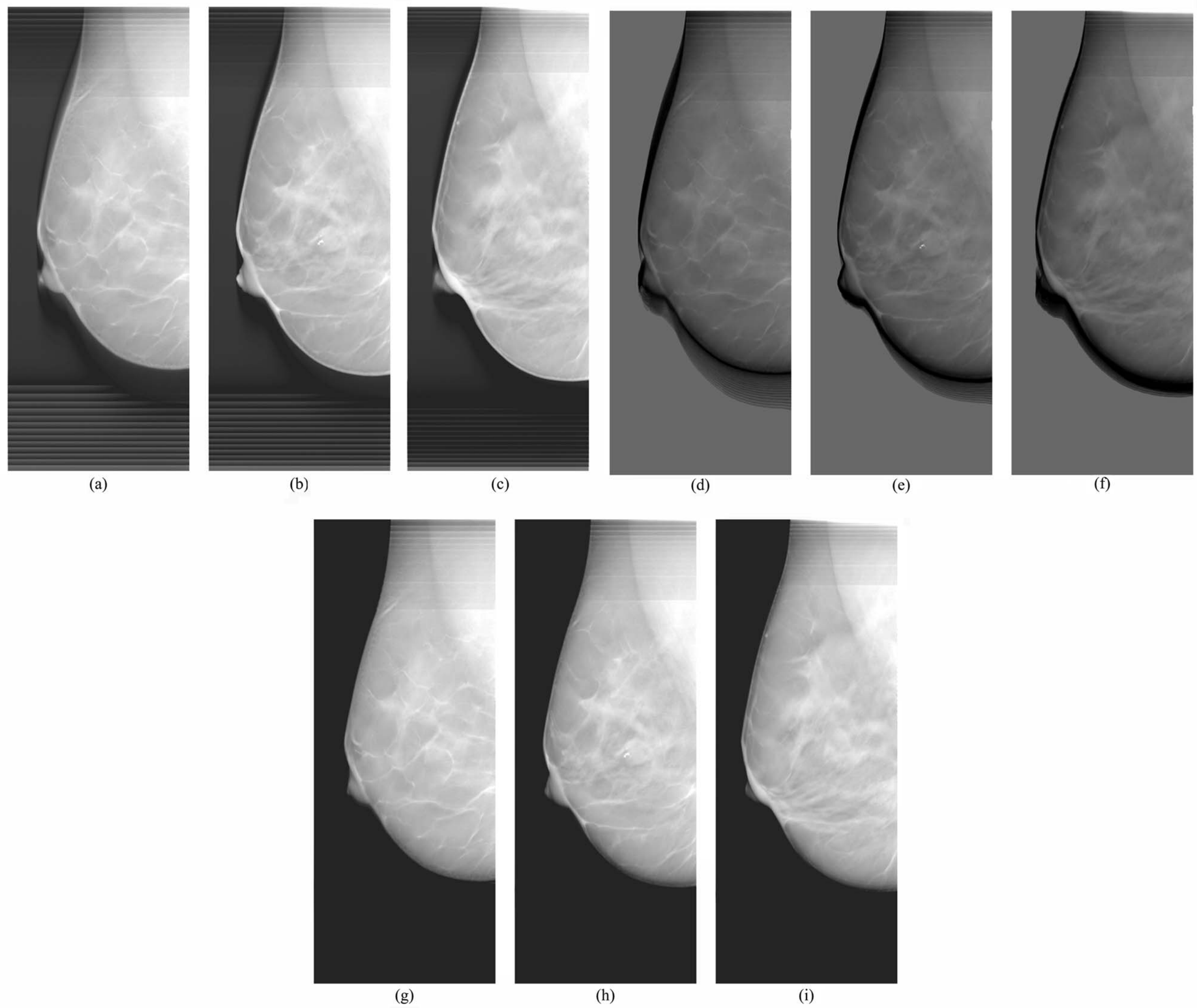

FIG. 10. Three selected tomosynthesized slice obtained by SART reconstruction for MLO view: (a), (d), and (g) 3.9 cm, (b), (e) and (h) 3.3 cm, (c), (f), and (i) 2.3 cm above the breast support plate; (a)–(c) reconstructed slices without using any breast boundary information, (d)–(f) reconstructed slices with using only 2D breast mask information (g)–(i) reconstructed slices with both the 2D and 3D breast boundary information. Note that with 2D breast mask, the detector boundary artifacts at the bottom have been eliminated while the breast boundary artifacts have been totally removed after application of the 3D breast shape. The skin lines are also less over-enhanced. The detector boundary artifacts at the top of the slice do not change because the tissue extended beyond the detector boundary. SART results with different methods ((a)–(c), (d)–(f), and (g)–(i)) are displayed with different window width and level to achieve visually comparable contrast of the boundary artifacts.

breast surface from the MLO view by using the proposed 3D conical trimming method.

Figure 10 shows examples of MLO-view DTM slices reconstructed with the SART method using one iteration and a relaxation parameter of 0.5. A constant distribution of voxel values was used as initialization. The DTM images reconstructed without using boundary information, as shown in (a)–(c); with only 2D breast mask information, as shown in (d)–(f); and with both 2D mask and 3D breast shape information, as shown in (g)–(i), were compared. The results of SART method with only 3D breast shape information should be the same as those with both 2D and 3D breast information, but one will not gain computational efficiency. The three chosen slices are 3.9, 3.3, and 2.3 cm above the breast support plate and the thickness of the imaged breast was measured by the DTM system as 5.4 cm. While the choice of these tomosynthesized slices was somewhat arbitrary, we attempt to choose slices that can clearly demonstrate the difference between the results with and without using breast boundary information. Note that in Figs. 10(d)–10(f), the background voxels retained the initialization constant as their values, which was chosen to be the average linear attenuation coefficient of normal breast tissues and was higher than those of the fatty tissue. In contrast, the exterior region outside the breast in Figs. 10(g)–10(i) were set to have values of zero, which was approximately the attenuation coefficient of air, after application of the 3D breast shape information.

Without using any breast boundary information, the detector boundary artifacts were clearly observed as multiple horizontal lines especially at the bottom of all three tomosynthe-

sized slices. At the top part of these slices, there were also detector boundary artifacts, as indicated by the PV-count map shown in Fig. 4, but the artifacts were much weaker than those at the bottom as a result of the PV access order, discussed above. The breast boundary artifacts, represented as repeated breast-shaped ghosts around the boundary, were clearly observed around the true breast boundary in-focus on each slice. The number of ghost shadows is 20 if the breast boundary is imaged in all 21 PVs because one boundary is in-focus and appears as real breast boundary at that depth.

The application of the generated 3D breast surface to the reconstructed slices removed all breast boundary artifacts. With the 2D breast mask information incorporated, the detector boundary artifacts outside the breast have been eliminated. More importantly, the skin lines in all DTM images are less over enhanced when the reconstruction is limited to the valid rays within the 2D breast boundary. The over-enhanced skin lines may create skin-thickening artifacts. The remaining detector artifacts within the generated breast surface, as shown at the top part of the slices, are due to the fact that the pectoral muscle was projected beyond the detector boundary at the large tomosynthesis angles, as shown in Fig. 8.

In this case, the computation time was reduced by 76.3% and 69.9% for the CC and MLO views, respectively, by using the 2D breast boundary masks for all PVs.

IV. DISCUSSION

We have investigated the application of the 2D and 3D breast boundary information to DTM reconstruction with the SART method. Preliminary results show that this method can substantially reduce the computation time and effectively remove the breast and detector boundary artifacts on tomosynthesized slices by employing only projection information from the rays intersecting the breast volume for reconstruction. When the breast boundary is completely inside the detector boundary, the use of valid rays only within the breast areas for reconstruction excludes the transition regions in the imaged volume that are covered by different number of PVs and enhanced during updating in subsequent PV processing. The detector boundary artifacts can thus be totally removed. When the projected breast image exceeds the detector area, the detector boundary artifacts outside the breast volume can be removed but those inside remain where the breast PV images are cut off by the detector boundary. After the SART reconstruction, breast boundary artifacts were removed by trimming off the air volume outside the 3D breast surface. The investigation of methods for reduction of the remaining artifacts will be undertaken in the future.

The 2D and 3D breast boundary information can be obtained prior to the reconstruction process. The 2D breast boundary curves are extracted from the individual PV images with a segmentation method developed in our laboratory. The 3D breast surface is generated by back projecting the 2D breast boundary curves sequentially followed by a 3D conical trimming process. The computational effort involved is trivial compared to the reconstruction procedure because only boundary pixels are needed to be back projected. Note that the 3D conical trimming method cannot recover parts of the breast surface where they overlap projected breast regions in all PV images. This will occur most likely in the region close to the gap between the breast support plate and the lower part, and between the compression plate and the upper part, around the boundary of the compressed breast, as indicated by dashed arrows in Fig. 3. The size of the breast surface area that cannot be recovered due to missing information will depend on the angular range of the DTM system, and the thickness and boundary curvature of the compressed breast. The larger the angular range of the DTM system, the smaller the missing gap.

The efficiency ratio is defined by dividing the average background area outside the detected breast boundary over all PV images by the detector area. Therefore the saving on the computational effort depends on the breast size of individual patient case and is greater for smaller breasts. To estimate the average saving on computational effort in a random sample of patient cases, we have calculated the efficiency ratio as the background area to detector area ratio for a data set of 96 two-view full field digital mammograms (FFDMs) acquired with a GE Senographe 2000D system, the detector of which has the same dimension as that of our prototype DTM system. This data set was collected previously in the Department of Radiology at the University of Michigan for our CAD study.[46] The resulting mean efficiency ratio for 96 CC-view FFDMs is 65.2% with a standard deviation of 14.7%; and the mean value for 96 MLO-view FFDMs is 56.0% with a standard deviation of 13.5%. While the average background area in the 21 PVs of a DTM will be slightly different from that of an FFDM, this should provide a good estimate of the efficiency ratio.

The developed 2D and 3D breast boundary information can be used in different ways with DTM reconstruction algorithms, rather than the one we described in this work. For example, with SART or other iterative methods, the 3D breast surface can be employed at different stages in the iterative process, e.g., masking the resulting imaged volume to allow setting all voxels outside the breast surface to air after each PV image has been used, rather than after all PV images have been used exactly once, as we suggested in this work. In terms of using object shape information in image reconstruction, Tam has presented a simple method to construct the convex hull of an imaged object in 2D limited-angle computerized tomography (CT) by intersecting or superimposing the back-projected object shadows.[47] He utilized this object support information in an iterative limited-angle CT reconstruction in which the missing PV images are estimated and used in a full-range FBP method. During the iterative process, the reconstructed object density distribution is improved by correcting the external volume to zero and applying other constraints to the density range.[48]

Another potential application of the 3D breast surface information is quantitative DTM reconstruction. In DTM reconstruction, the air volume outside the breast, if not excluded, will affect the estimation of the average attenuation value back projected to the real breast volume. With the 3D

breast surface information, if only the pathlength within the real breast volume will be taken into account in calculating the x-ray attenuation properties of the breast tissues, it will provide potential improvement in quantitative estimation of the linear attenuation coefficients.

In addition to applications in DTM reconstruction, the 3D breast surface and volume information will be useful for breast density estimation. Breast density has been shown to be an important risk factor for breast cancer. The change in breast density is considered a useful surrogate for estimating the change in breast cancer risk due to treatment or intervention. Currently the change in breast density is monitored mainly by estimating the change in the dense area on conventional projection mammograms. Because of the projection of the 3D volume to a 2D plane, the percentage of dense area on a mammogram does not accurately reflect the percentage of dense tissue in the breast volume although a strong correlation has been demonstrated.[49] It can be expected that 3D volumetric information available from DTM will provide a better estimation of the amount of dense tissue in the breast volume and its changes over time than projection mammograms.

V. CONCLUSION

In this study, we have applied the 2D breast boundary information and the generated 3D breast surface to SART reconstruction in breast tomosynthesis mammography. The 2D breast boundary is detected on the projection view images using a boundary tracking algorithm developed in our laboratory and the 3D breast surface is generated with a 3D conical trimming method. The 2D breast boundary curves on PV images are used to restrict the SART reconstruction to be performed only inside the breast area while the 3D breast surface is used to exclude reconstruction artifacts outside the breast volume. Experimental results with patient PV images demonstrated that the proposed method can substantially improve computational efficiency by eliminating unnecessary reconstruction in regions outside the breast. Both breast boundary and detector boundary artifacts can be effectively removed by the proposed method.

ACKNOWLEDGMENTS

This work is supported by USPHS Grant Nos. CA120234, CA91713 and CA95153, and U.S. Army Medical Research and Materiel Command Grant Nos. W81XWH-07-1-0324 and DAMD 17-02-1-0214. The content of this paper does not necessarily reflect the position of the funding agencies and no official endorsement of any equipment and product of any companies mentioned should be inferred. The digital tomosynthesis system was developed by the GE Global Research Group through the Biomedical Research Partnership (USPHS Grant No. CA91713) collaboration.

[a]Electronic mail: yihzhang@med.umich.edu

[1]L. T. Niklason *et al.*, "Digital tomosynthesis in breast imaging," Radiology **205**, 399–406 (1997).
[2]T. Wu *et al.*, "Tomographic mammography using a limited number of low-dose cone-beam projection images," Med. Phys. **30**, 365–380 (2003).
[3]S. Suryanarayanan, A. Karellas, S. Vedantham, S. J. Glick, C. J. D'Orsi, S. P. Baker, and R. L. Webber, "Comparison of tomosynthesis methods used with digital mammography," Acad. Radiol. **7**, 1085–1097 (2000).
[4]S. Suryanarayanan, A. Karellas, S. Vedantham, S. P. Baker, S. J. Glick, C. J. D'Orsi, and R. L. Webber, "Evaluation of linear and nonlinear tomosynthetic reconstruction methods in digital mammography," Acad. Radiol. **8**, 219–224 (2001).
[5]J. W. Eberhard *et al.*, "High speed, large angle mammography tomosynthesis system," Proc. SPIE **6142**, 61420C (2006).
[6]D. Kopans, "Digital tomosynthesis and other applications," RSNA Program Book 2005 130 (2005).
[7]E. Rafferty, "Breast tomosynthesis," RSNA Program Book 2005 141 (2005).
[8]M. A. Helvie, M. A. Roubidoux, Y. Zhang, P. L. Carson, and H.-P. Chan, "Tomosynthesis mammography vs conventional mammography: Lesion detection and reader preference. Initial experience," RSNA Program Book 2006 335 (2006).
[9]B. Ren, C. Ruth, J. Stein, A. Smith, I. Shaw, and Z. Jing, "Design and performance of the prototype full field breast tomosynthesis system with selenium based flat panel detector," Proc. SPIE **5745**, 550–561 (2005).
[10]M. Bissonnette *et al.*, "Digital breast tomosynthesis using an amorphous selenium flat panel detector," Proc. SPIE **5745**, 529–540 (2005).
[11]S. Poplack, C. Kogel, and H. Nagy, "Initial experience with digital breast tomosynthesis in 99 breasts of 98 women with abnormal digital screening mammography," RSNA Program Book 2005 317 (2005).
[12]R. Moore, A. Stewart, T. Wu, D. Kopans, E. Rafferty, and D. Georgian-Smith, "Second-generation digital breast tomosynthesis (DBT) in the screening setting: Workflow and preliminary results," RSNA Program Book 2005 318 (2005).
[13]J. Lo, J. Baker, J. Orman, T. Mertelmeier, and S. Singh, "Breast tomosynthesis: Initial clinical experience with 100 human subjects," RSNA Program Book 2006 335 (2006).
[14]D. G. Grant, "Tomosynthesis: A three-dimensional radiographic imaging technique," IEEE Trans. Biomed. Eng. **19**, 20–28 (1972).
[15]Z. Kolitsi, G. Panayiotakis, V. Anastassopoulus, A. Scodras, and N. Pallikarakis, "A multiple projection method for digital tomosynthesis," Med. Phys. **19**, 1045–1050 (1992).
[16]A. Kak and M. Slaney, *Principle of Computerized Tomographic Imaging* (IEEE, New York, 1988).
[17]G. Lauritsch and W. Haerer, "A theoretical framework for filtered backprojection in tomosynthesis," Proc. SPIE **3338**, 1127–1137 (1998).
[18]H. Matsuo, A. Iwata, I. Horiba, and N. Suzumura, "Three-dimensional image reconstruction by digital tomosynthesis using inverse filtering," IEEE Trans. Med. Imaging **12**, 307–313 (1993).
[19]T. Mertelmeier, J. Orman, W. Haerer, and M. K. Dudam, "Optimizing filtered backprojection reconstruction for a breast tomosynthesis prototype device," Proc. SPIE **6142**, 61420F (2006).
[20]J. T. Dobbins III and D. J. Godfrey, "Digital x-ray tomosynthesis: Current state of the art and clinical potential," Phys. Med. Biol. **48**, R65–R106 (2003).
[21]R. J. Warp, D. J. Godfrey, and J. T. Dobbins III, "Applications of matrix inverse tomosynthesis," Proc. SPIE **3977**, 376–383 (2000).
[22]Y. Chen, J. Y. Lo, J. A. Baker, and J. T. Dobbins III, "Gaussian frequency blending algorithm with matrix inversion tomosynthesis (MITS) and filtered back projection (FBP) for better digital breast tomosynthesis reconstruction," Proc. SPIE **6142**, 122–130 (2006).
[23]B. Wang, K. Barnera, and D. Leeb, "Algebraic tomosynthesis reconstruction," Proc. SPIE **5370**, 711–718 (2004).
[24]A. H. Andersen and A. C. Kak, "Simultaneous algebraic reconstruction technique (SART): A new implementation of the ART algorithm," Ultrason. Imaging **6**, 81–94 (1984).
[25]Y. Zhang, H.-P. Chan, B. Sahiner, J. Wei, M. M. Goodsitt, L. M. Hadjiiski, J. Ge, and C. Zhou, "A comparative study of limited-angle cone-beam reconstruction methods for breast tomosynthesis," Med. Phys. **33**, 3781–3795 (2006).
[26]K. Lange and J. A. Fessler, "Globally convergent algorithms for maximum a posteriori transmission tomography," IEEE Trans. Image Process. **4**, 1430–1438 (1995).
[27]T. Wu, J. Zhang, R. Moore, E. Rafferty, and D. Kopans, "Digital tomosynthesis mammography using a parallel maximum-likelihood reconstruction method," Proc. SPIE **5368**, 1–11 (2004).
[28]U. E. Ruttimann, R. A. J. Groenhuis, and R. L. Webber, "Restoration of digital multiplane tomosynthesis by a constrained iteration method,"

IEEE Trans. Med. Imaging **MI-3**, 141–148 (1984).

[29]D. N. G. Roy, R. A. Kruger, B. Yih, and P. D. Rio, "Selective plane removal in limited angle tomographic imaging," Med. Phys. **12**, 65–70 (1985).

[30]Z. Kolitsi, G. Panayiotakis, and N. Pallikarakis, "A method for selective removal of out-of-plane structures in digital tomosynthesis," Med. Phys. **20**, 47–50 (1993).

[31]J. Ge, H.-P. Chan, B. Sahiner, Y. Zhang, J. Wei, L. M. Hadjiiski, and C. Zhou, "Digital tomosynthesis mammography: Intra- and interplane artifact reduction for high-contrast objects on reconstructed slices using a priori 3D geometrical information," Proc. SPIE **6512**, 65124Q (2007).

[32]P. Haaker, E. Klotz, R. Koppe, R. Linde, and H. Moller, "A new digital tomosynthesis method with less artifacts for angiography," Med. Phys. **12**, 431–436 (1985).

[33]B. E. H. Claus and J. W. Eberhard, "A new method for 3D reconstruction in digital tomosynthesis," Proc. SPIE **4684**, 814–824 (2002).

[34]T. Wu, R. H. Moore, and D. B. Kopans, "Voting strategy for artifact reduction in digital breast tomosynthesis," Med. Phys. **33**, 2461–2471 (2006).

[35]I. Goddard, T. Wu, S. Thieret, A. Berman, and H. Bartsch, "Implementing an iterative reconstruction algorithm for digital breast tomosynthesis on graphics processing hardware," Proc. SPIE **6142**, 61424V (2006).

[36]H.-P. Chan, J. Wei, T. Wu, B. Sahiner, E. A. Rafferty, L. M. Hadjiiski, M. A. Helvie, M. A. Roubidoux, R. H. Moore, and D. B. Kopans, "Computer-aided detection on digital breast tomosynthesis (DBT) mammograms - dependence on image quality of reconstruction," RSNA Program Book 269 (2005).

[37]R. L. Siddon, "Fast calculation of the exact radiological path for a three-dimensional CT array," Med. Phys. **12**, 252–255 (1985).

[38]T. Wu, R. H. Moore, E. A. Rafferty, and D. B. Kopans, "A comparison of reconstruction algorithms for breast tomosynthesis," Med. Phys. **31**, 2636–2647 (2004).

[39]C. Zhou, H.-P. Chan, C. Paramagul, M. A. Roubidoux, B. Sahiner, L. M. Hadjiiski, and N. Petrick, "Computerized nipple identification for multiple image analysis in computer-aided diagnosis," Med. Phys. **31**, 2871–2882 (2004).

[40]Y.-T. Wu, C. Zhou, L. M. Hadjiiski, J. Shi, C. Paramagul, B. Sahiner, and H.-P. Chan, "A dynamic multiple thresholding method for automated breast boundary detection in digitized mammograms," Proc. SPIE **6512**, 65122U (2007).

[41]N. Otsu, "A threshold selection method from gray-level histograms," IEEE Trans. Syst. Man Cybern. **9**, 62–66 (1979).

[42]A. H. Andersen, "Algebraic reconstruction in CT from limited views," IEEE Trans. Med. Imaging **8**, 50–55 (1989).

[43]R. Gordon, R. Bender, and G. T. Herman, "Algebraic reconstruction techniques (ART) for three dimensional electron microscopy and x-ray photography," J. Theor. Biol. **29**, 471–481 (1970).

[44]G. T. Herman, *Image Reconstruction from Projections: The Fundamentals of Computerized Tomography* (Academic, New York, 1980).

[45]Y. Zhang, H.-P. Chan, B. Sahiner, J. Wei, L. M. Hadjiiski, J. Ge, and C. Zhou, "Breast tomosynthesis reconstruction with simultaneous algebraic reconstruction technique (SART): Effect of access strategy of projection-view images," RSNA Program Book 130 (2006).

[46]J. Ge, B. Sahiner, L. M. Hadjiiski, H.-P. Chan, J. Wei, M. A. Helvie, and C. Zhou, "Computer aided detection of clusters of microcalcifications on full field digital mammograms," Med. Phys. **33**, 2975–2988 (2006).

[47]K. C. Tam, "The construction and use of convex hulls in limited-angle computerized tomography," J. Nondestruct. Eval. **6**, 189–204 (1987).

[48]K. C. Tam and V. Perez-Mendez, "Tomographical imaging with limited-angle input," J. Opt. Soc. Am. **71**, 582–592 (1981).

[49]J. Wei, H.-P. Chan, M. A. Helvie, M. A. Roubidoux, B. Sahiner, L. Hadjiiski, C. Zhou, S. Paquerault, T. Chenevert, and M. M. Goodsitt, "Correlation between mammographic density and volumetric fibroglandular tissue estimated on breast MR images," Med. Phys. **31**, 933–942 (2004).

Truncation Artifact and Boundary Artifact Reduction in Breast Tomosynthesis Reconstruction

Yiheng Zhang*, Heang-Ping Chan, Yi-Ta Wu, Berkman Sahiner, Chuan Zhou, Jun Wei, Jun Ge, Lubomir M. Hadjiiski, Jiazheng Shi

Department of Radiology, University of Michigan, Ann Arbor, MI 48109

ABSTRACT

Digital Tomosynthesis Mammography (DTM) is an emerging technique that has the potential to improve breast cancer detection. DTM acquires low-dose mammograms at a number of projection angles over a limited angular range and reconstructs the 3D breast volume. Due to the limited number of projections within a limited angular range and the finite size of the detector, DTM reconstruction contains boundary and truncation artifacts that degrade the image quality of the tomosynthesized slices, especially that of the boundary and truncated regions. In this work, we developed artifact reduction methods that make use of both 2D and 3D breast boundary information and local intensity-equalization and tissue-compensation techniques. A breast phantom containing test objects and a selected DTM patient case were used to evaluate the effects of artifact reduction. The contrast-to-noise ratio (CNR), the normalized profiles of test objects, and a non-uniformity error index were used as performance measures. A GE prototype DTM system was used to acquire 21 PVs in 3º increments over a ±30º angular range. The Simultaneous Algebraic Reconstruction Technique (SART) was used for DTM reconstruction. Our results demonstrated that the proposed methods can improve the image quality both qualitatively and quantitatively, resulting in increased CNR value, background uniformity and an overall reconstruction quality comparable to that without truncation. For the selected DTM patient case, the obscured breast structural information near the truncated regions was essentially recovered. In addition, restricting SART reconstruction to be performed within the estimated 3D breast volume increased the computation efficiency.

Keywords: Digital Tomosynthesis Mammography (DTM), Simultaneous Algebraic Reconstruction Technique (SART), truncation artifacts, boundary artifacts.

1. INTRODUCTION

Digital tomosynthesis mammography (DTM) is an emerging technique that can provide volumetric information for breast imaging by reconstructing the breast volume from multiple low-dose projection views acquired at a number of angles in a limited angular range[1,2]. The total radiation dose is set to be comparable to that used in regular screening mammography. DTM reconstruction is therefore a limited-angle cone-beam tomographic problem. We previously demonstrated that the Simultaneous Algebraic Reconstruction Technique (SART) method can achieve high image quality[3]. However, the reconstructed DTM slices contain strong boundary and truncation artifacts due to the limited angular range and the truncated projection-view (PV) images. Moreover, iterative reconstruction algorithm such as SART requires extensive computation, therefore it is of practical importance to improve computational efficiency.

* yihzhang@umich.edu, Tel: 734-647-8556, C474 Med-Inn Bldg, 1500 E. Medical Center Dr., Ann Arbor, MI 48109.

Medical Imaging 2008: Physics of Medical Imaging, edited by Jiang Hsieh, Ehsan Samei,
Proc. of SPIE Vol. 6913, 69132Y, (2008) · 1605-7422/08/$18 · doi: 10.1117/12.769698

In this work, our purpose is to develop methods to reduce both truncation and boundary artifacts, improve reconstruction image quality in the truncated region, and enhance computational efficiency of the SART method.

2. METHODS

2.1 DTM SYSTEM

A GE prototype DTM system was used to acquire 21 PVs in 3º increments over a ±30º angular range. The imaging geometry of this DTM system is schematically shown in Figure 1. Institutional Review Board (IRB) approval and informed consent were obtained for patient cases. The distance from the x-ray focal spot to the center of rotation is 64 cm and the plane along which the x-ray source rotates is perpendicular to the detector surface at the chest wall edge. The focal-spot-to-detector distance is 66 cm. The system has a CsI phosphor/a:Si active matrix flat panel digital detector with a pixel size of 0.1 mm×0.1 mm and 16 bits per pixel. The image acquisition process takes less than 8 seconds and the digital detector (X-Y plane) is stationary during image acquisition.

In our previous work[3], we have compared different methods for DTM reconstruction based on breast phantom study and demonstrated that the SART method[5] can provide high-quality tomosynthesized slices while being more efficient than the maximum likelihood method[2]. In this study, SART was employed for DTM reconstruction. The imaged volume was subdivided into a set of voxels, of which the X and Y dimensions were set to be the same as the detector pixel size, i.e., 0.1 mm, and the Z dimension (slice thickness) was chosen to be 1.0 mm. In SART, an update of the attenuation properties of the imaged volume is performed based on each PV and the iteration process starts with an initial distribution. The value of each voxel is updated after all rays in one projection view have been processed. We used SART with one iteration, i.e. using all PV images exactly once, in this study. The relaxation parameter was set to be 0.5 for all PVs.

2.2 BOUNDARY ARTIFACT REDUCTION

The 2D breast boundary on each PV image is segmented by a breast boundary detection program developed in our laboratory[6]. There are two main steps in the algorithm: detection of an initial breast boundary by applying Otsu's thresholding[7] to the histogram of the PV image, followed by a boundary tracking procedure based on gradient information obtained from both horizontal and vertical Sobel filtering. With the detected 2D breast boundary curves on all PV images, a 3D breast surface can be generated to enclose the compressed breast while excluding the exterior air space. We implemented a "3D conical trimming" process to recover the unique convex hull inside the 3D imaged volume of which the projections at different angles precisely correspond to the breast shadow on each PV image. Specifically, for a given PV image, the breast boundary curve is back-projected into the imaged volume and all "air-volume" outside the generated conical surface formed by the x-ray source and the breast boundary is trimmed off. This process is performed for all PV images. The intersection of the conical surfaces from all PV breast boundary curves forms the desired convex hull. The convex hull combined with the top and bottom surfaces of the breast delineated by the compression paddle and the breast support plate define an enclosed breast volume.

To apply the breast boundary information to DTM reconstruction using the SART method, we restrict the re-projection and the back-projection of the difference between the calculated data and the measured data to be performed along those "valid" rays within the 2D breast area only. After one complete SART iteration has been performed, we use the 3D breast surface to mask the resulting volume and set the

values of all voxels outside the breast surface to that of air. This will remove all boundary artifacts, including those from the breast boundary and the detector boundary outside the breast volume. The computational effort is reduced by eliminating the processing of all rays outside the breast region on each individual PV. Detailed description of this method can be found in our recent publication[8].

2.3 TRUNCATION ARTIFACT REDUCTION

When a portion of the breast is not recorded in some or all of the PV images because of a finite-size detector, the truncated projections will cause artifacts in DTM reconstruction. The limited field of view (FOV) results in unexposed regions in the imaged volume and truncation of the PVs, particularly at large projection angles. In iterative reconstruction such as SART, the imaged volume is updated by processing each individual PV image, i.e. only the part of the imaged volume within the cone-beam ray path of the current PV will be updated. This will result in discontinuity in the voxel values across the cone-beam path boundary which will be enhanced by further PV processing in the same and subsequent iterations. These artifacts, referred to as “detector boundary” truncation artifacts, appear as bright staircase-like lines or bands at the two sides perpendicular to the x-ray source motion on all tomosynthesized slices.

A second source of truncation artifacts is caused by the missed portion of breast tissue that is outside the finite imaged volume modeled in the reconstruction algorithm. The missed tissue volume will cause estimation error in the x-ray attenuation. Since the attenuation will be considered to have occurred only within the shortened pathlength, the voxel values will be overestimated. The overestimated attenuation results in bright voxels and will be referred to as “glaring” artifact.

Both of these truncation artifacts are apparent mainly at the image boundary of DTM slices. They will obscure the breast tissue details near the boundary of DTMs, potentially affecting the accuracy of lesion detection. These artifacts cannot be eliminated by using the breast boundary information alone. We have developed correction techniques to reduce their visibility.

For truncation artifact reduction, a local intensity-equalization method was developed to suppress the discontinuity of the reconstructed voxel intensity. Specifically, for each PV image, after the updating using the current PV is completed, we replace all voxel values within the oblique wedge-shape volume with some average values obtained from their neighborhood region. This procedure is implemented in a column-wise manner, i.e., along each column of voxels parallel to the Y-axis on every tomosynthesized slice. To reduce the glaring artifact, we designed a practical tissue-compensation method. For any x-ray incident on the preset rectangular imaged volume from the boundary side, it is assumed that this ray has encountered very large attenuation if the corresponding detected x-ray intensity is below a predetermined threshold. The computed total attenuation of this ray will be compensated for by assuming that the missing volume is filled with “average” breast tissue. In addition, the modified difference between the detected data and the new computed data is normalized by the compensated total pathlength but back-projected only to those voxels within the preset imaged volume.

2.4 BREAST PHANTOM AND FIGURES OF MERIT

To quantitatively evaluate the improvement in image quality by artifact correction, a custom-built breast phantom was used which contained test objects on a thin feature layer sandwiched between homogeneous Lucite plates. The test objects were arranged in groups in both the boundary and middle regions, as schematically shown in Figure 2. The test objects included layers of thin circular aluminum foils to simulate masses, high-contrast metal wires to simulate metal markers, and low-contrast plastic wires to

simulate speculations. The two groups of masses, denoted by M1, M2 and M3 and by M4, M5 and M6 respectively, differ in the number of aluminum foils to simulate different contrasts. The lower-contrast masses are drawn with a slightly smaller size than those for the higher-contrast ones although they have the same diameter in reality.

The contrast-to-noise ratio (CNR), the normalized line profiles of feature objects, and a non-uniformity error index are used as performance measures to compare the image quality of the test objects near the detector boundary with and without applying the artifact reduction methods, and to the image quality of the test objects in the middle region where no truncation occurred. The CNR of the simulated mass is defined as the difference in the average pixel intensities between the mass and its local image background, divided by the standard deviation of pixel intensity in the same background. The non-uniformity error index (NUEI) is defined as the ratio of the difference between the average pixel intensities of two ROIs located in the middle region and the lower boundary region, respectively, to the average pixel intensity of the middle region. Both ROIs in the boundary and the middle regions were chosen to be homogeneous Lucite background containing no objects.

3. RESULTS

For the breast phantom study, the number of PV images in which the group of test objects in the lower boundary region (i.e., M1, W1, M4 and W4) was truncated was 8 to 9. Figure 3 shows the reconstruction results of the lower part of the feature layer with and without the truncation artifact reduction. Results of the upper and middle groups of features were not shown because they were not affected by the proposed methods. The detector boundary artifacts appearing as bright horizontal lines have been totally removed. The visual image quality of all features was markedly improved, especially for the low-contrast plastic wire that was almost totally obscured by the truncation artifacts without correction. The line profiles of all simulated masses are shown in Figure 4, in which the high- and low-contrast mass groups are shown separately. In each group, the line profiles of the object located in the lower region (e.g., M1), without and with artifact reduction, were plotted together with the line profiles of the counterpart object in the middle region (e.g., M2) and the top region (e.g., M3). For masses, all line profiles were mean-removed. It can be seen that the line profiles of all masses located in the lower region contained strong truncation artifacts (i.e. large discontinuities) without artifact reduction. With artifact reduction, the resulting line profiles were much smoother, similar to that of the counterpart object in the middle region where no truncation occurred. The CNR values of the simulated masses and the NUEI values are listed in Table 1 where the numbers in the parentheses are the results without artifact reduction. The NUEI values indicate that the artifact reduction methods improved the uniformity in the reconstructed homogeneous Lucite background. The improvement in the CNR values of masses M1 and M4 is substantial.

For the selected patient DTM case, a mediolateral oblique (MLO) view with truncated PV images was used. The #1, #11 and #21 raw PV images, corresponding to the projection angles -30°, 0°, +30°, are shown in Figures 5. The x-ray source moved in the vertical direction relative to the images shown. Figure 6 shows the generated 3D breast surface by using the proposed 3D conical trimming method. Figure 7 shows examples of DTM slices reconstructed with the SART method for which a constant distribution of voxel values was used as initialization. The DTM images reconstructed without using any artifact reduction (top row) and with both boundary and truncation artifact reduction (bottom row) were compared. The three chosen slices are 3.1 cm, 2.1 cm, and 0.8 cm above the breast support plate and the thickness of the imaged breast was measured by the DTM system as 4.9 cm. Without using any artifact reduction, the detector boundary artifacts were observed as multiple horizontal lines especially at the top of all three tomosynthesized slices. The breast boundary artifacts, represented as repeated breast-shape ghosts around the

boundary, were clearly observed around the true breast boundary in-focus on each slice. It is also evident that both the detector boundary artifact and glaring artifact strongly degraded the visibility of the breast structures in the boundary areas that were close to the pectoral muscle where the PV images were severely truncated. The correction methods removed all breast boundary artifacts, effectively suppressed the truncation artifacts and recovered the local breast tissue details. The glaring artifacts caused by the truncated pathlengths have been corrected and the reconstructed voxel intensities are similar to those of normal breast tissue. In this case, the computation time was reduced by 63.2% by using the 2D breast boundary masks, compared to full-field processing.

4. DISCUSSION AND CONCLUSION

DTM can provide quasi-3D information in breast imaging in contrast to conventional mammography. However, due to the limited number of projections within a limited angular range and the finite size of the flat panel detector, DTM reconstruction contains boundary and truncation artifacts that degrade the image quality of the tomosynthesized slices, especially in the boundary and truncated regions. In this study, we developed artifact reduction methods and evaluated the improvement on breast phantom images and DTM patient case. Our results indicated that, based on the SART method for the limited-angle cone-beam 3D reconstruction, the proposed methods can substantially reduce the artifacts, improve the image quality both qualitatively and quantitatively, and provide reconstruction quality comparable to that without truncation. In addition, the computation time of SART is reduced substantially by using the 2D breast boundary information. Further work is underway to investigate the generalizability of the correction methods to other reconstruction techniques and the correction of artifacts that are caused by high-attenuation objects.

ACKNOWLEGMENTS

This work is supported by U. S. Army Medical Research and Materiel Command grant W81XWH 07-1-0324, and USPHS grants CA120234, CA91713 and CA95153. The content of this paper does not necessarily reflect the position of the funding agencies and no official endorsement of any equipment and product of any companies mentioned should be inferred. The digital tomosynthesis system was developed by the GE Global Research Group through the Biomedical Research Partnership (USPHS grant CA91713) collaboration.

REFERENCES

1. L. T. Niklason, B. T. Christian, L. E. Niklason, D. B. Kopans, D. E. Castleberry, B. H. Opsahl-Ong, C. E. Landberg, P. J. Slanetz, A. A. Giardino, R. Moore, D. Albagli, M. C. Dejule, F. C. Fitzgerald, D. F. Fobare, B. W. Giambattista, R. F. Kwasnick, J. Liu, S. J. Lubowski, G. E. Possin, J. F. Richotte, W. C. Y. and R. F. Wirth, "Digital tomosynthesis in breast imaging," *Radiology* **205**, 399-406, 1997.
2. T. Wu, A. Stewart, M. Stanton, T. Mccauley, W. Phillips, D. B. Kopans, R. H. Moore, J. W. Eberhard, B. Opsahl-Ong, L. Niklason and M. B. Williams, "Tomographic mammography using a limited number of low-dose cone-beam projection images," *Medical Physics* **30**, 365-380, 2003.
3. Y. Zhang, H.-P. Chan, B. Sahiner, J. Wei, M. M. Goodsitt, L. M. Hadjiiski, J. Ge and C. Zhou, "A comparative study of limited-angle cone-beam reconstruction methods for breast tomosynthesis," *Medical Physics* **33**, 3781-3795, 2006.
4. J. W. Eberhard, P. Staudinger, J. Smolenski, J. Ding, A. Schmitz, J. McCoy, M. Rumsey, A. Al-Khalidy, W. Ross, C. E. Landberg, B. E.H. Claus, P. Carson, M. Goodsitt, H.-P. Chan, M. Roubidoux, J. A. Thomas and J. Osland, "High Speed, Large Angle Mammography Tomosynthesis System," *Proc SPIE* **6142**, 0C1-0C11, 2006.

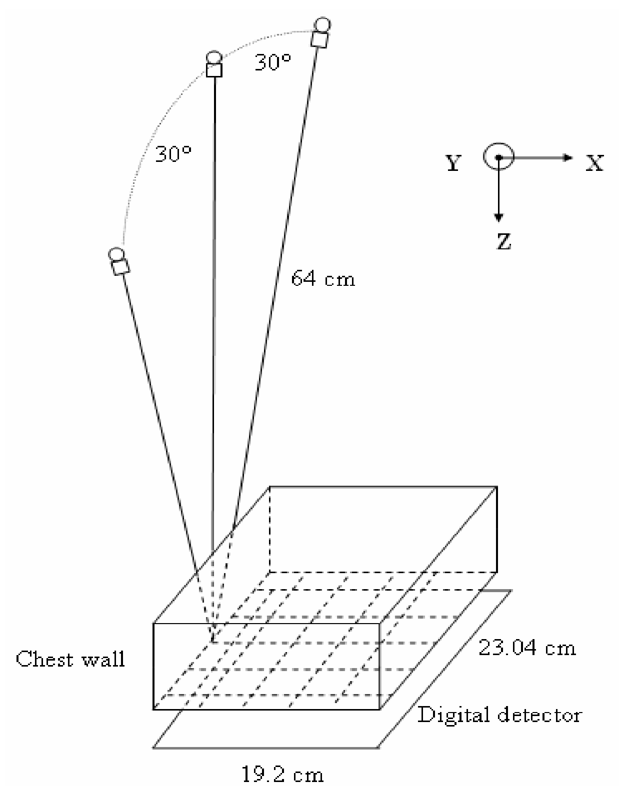
30°
30°
64 cm
Y
X
Z
Chest wall
23.04 cm
Digital detector
19.2 cm

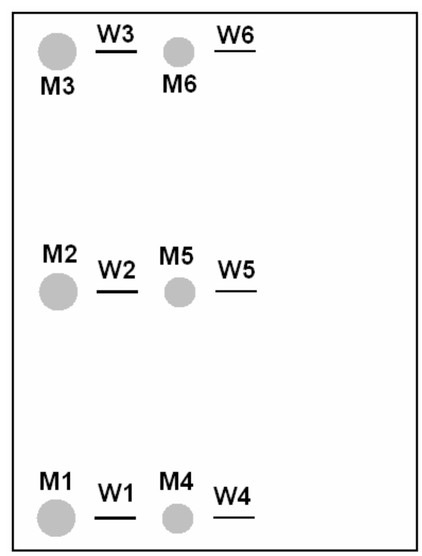
W3
W6
M3
M6
M2
W2
M5
W5
M1
W1
M4
W4

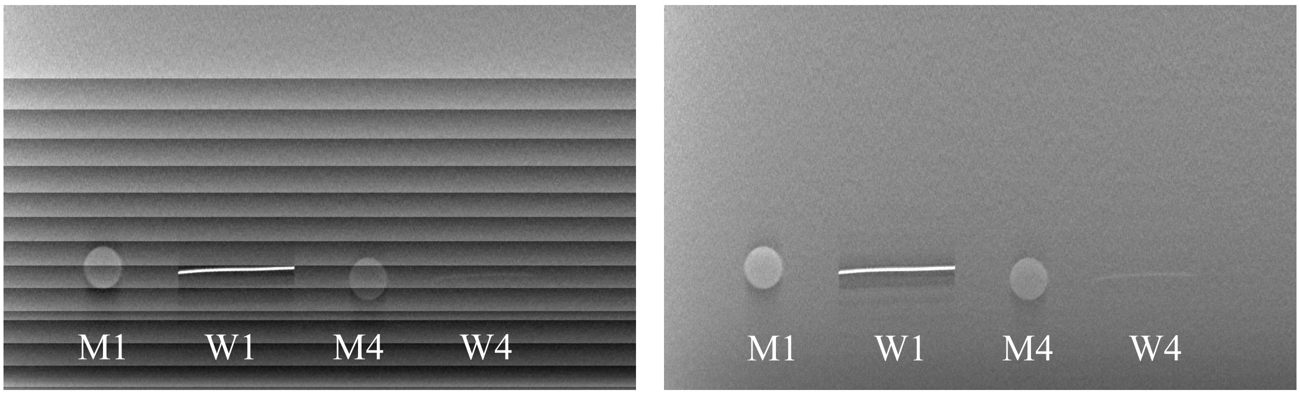

Figure 3. SART reconstructed DTM slice of the phantom feature layer, without (left) and with (right) the artifact reduction. Only the lower region was shown and the corresponding test objects are indicated.

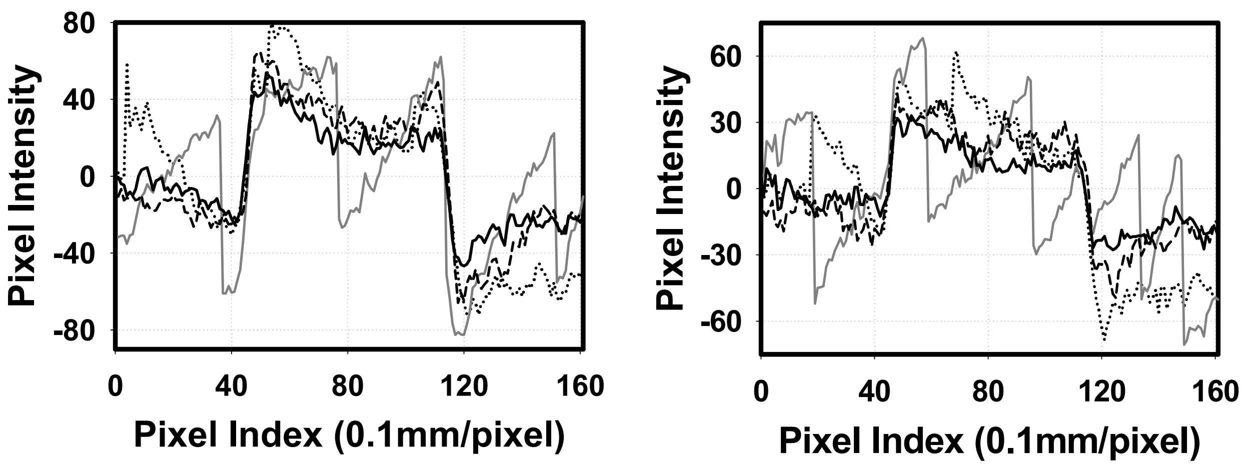

(a) M1, M2 and M3

(b) M4, M5 and M6

Figure 4. Comparison of the normalized line profiles of all simulated masses: the feature located in the lower region, without (solid gray line) and with artifact reduction (solid black line), the corresponding feature located in the middle (black dashed line) and the top (black dotted line) regions. The pixel intensity was normalized by removing the mean of each line profile.

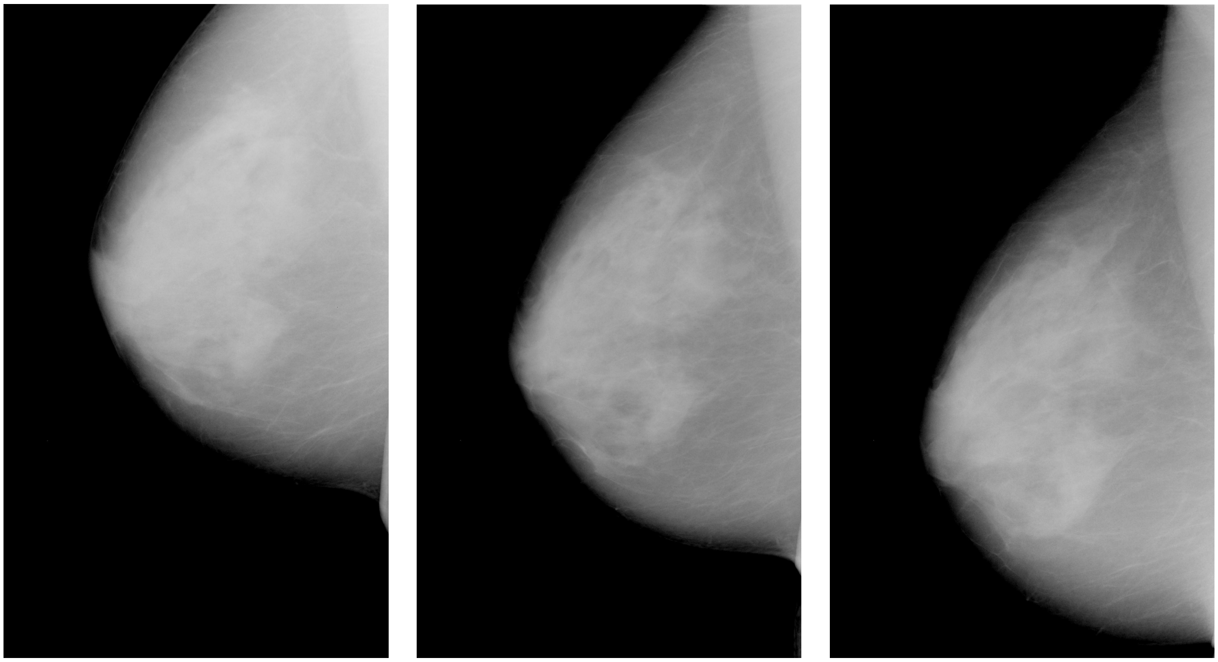

Figure 5. Projection view images of a DTM patient case in MLO view: PV at -30° (left), PV at 0° (middle) and PV at +30° (right). The x-ray source moved in the vertical direction relative to the images shown.

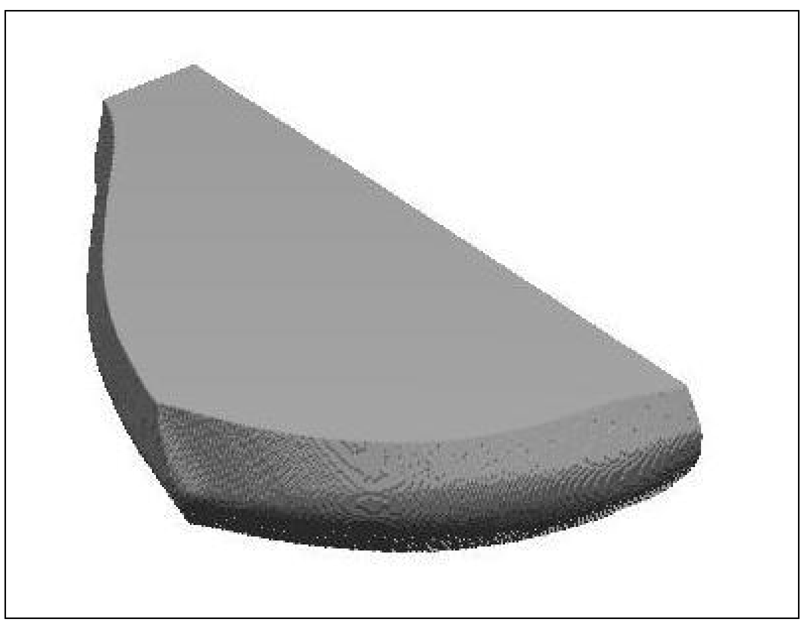

Figure 6. The 3D breast surface generated from 2D breast boundary curves by using the 3D conical trimming method.

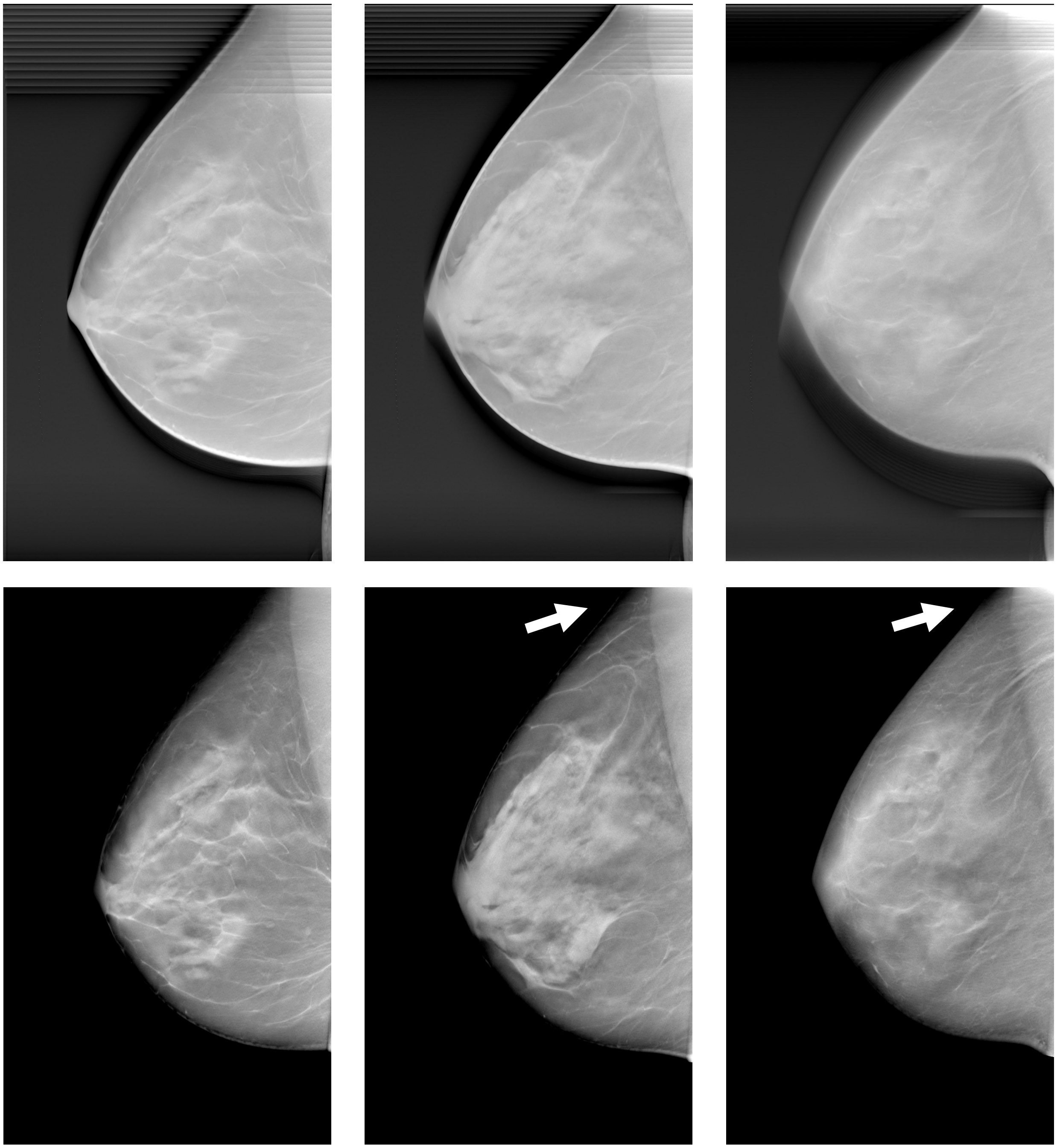

Classification of breast masses and normal tissues in digital tomosynthesis mammography

Jun Wei*, Heang-Ping Chan, Yiheng Zhang, Berkman Sahiner, Chuan Zhou,
Jun Ge, Yi-Ta Wu, Lubomir M. Hadjiiski

Department of Radiology, The University of Michigan, Ann Arbor, MI 48109

ABSTRACT

Digital tomosynthesis mammography (DTM) can provide quasi-3D structural information of the breast by reconstructing the breast volume from projection views (PV) acquired in a limited angular range. Our purpose is to design an effective classifier to distinguish breast masses from normal tissues in DTMs. A data set of 100 DTM cases collected with a GE first generation prototype DTM system at the Massachusetts General Hospital was used. We reconstructed the DTMs using a simultaneous algebraic reconstruction technique (SART). Mass candidates were identified by 3D gradient field analysis. Three approaches to distinguish breast masses from normal tissues were evaluated. In the 3D approach, we extracted morphological and run-length statistics texture features from DTM slices as input to a linear discriminant analysis (LDA) classifier. In the 2D approach, the raw input PVs were first preprocessed with a Laplacian pyramid multi-resolution enhancement scheme. A mass candidate was then forward-projected to the preprocessed PVs in order to determine the corresponding regions of interest (ROIs). Spatial gray-level dependence (SGLD) texture features were extracted from each ROI and averaged over 11 PVs. An LDA classifier was designed to distinguish the masses from normal tissues. In the combined approach, the LDA scores from the 3D and 2D approaches were averaged to generate a mass likelihood score for each candidate. The A_z values were 0.87±0.02, 0.86±0.02, and 0.91±0.02 for the 3D, 2D, and combined approaches, respectively. The difference between the A_z values of the 3D and 2D approaches did not achieve statistical significance. The performance of the combined approach was significantly ($p<0.05$) better than either the 3D or 2D approach alone. The combined classifier will be useful for false-positive reduction in computerized mass detection in DTM.

Keywords: Digital Tomosynthesis Mammography (DTM), Simultaneous Algebraic Reconstruction Technique (SART), Breast mass, Receiver operating characteristic (ROC) analysis

1. INTRODUCTION

Breast cancer is one of the leading causes of cancer mortality among women[1]. Although mammography is a powerful screening tool for detecting breast cancer, the sensitivity of cancer detection is often limited by the presence of the overlapping dense fibroglandular tissue in the breast. Digital tomosynthesis mammography (DTM) is one of the new breast imaging modalities that have potential to improve the detection and diagnosis of breast cancer. In DTM, a serial of low-dose projection view images (PVs) are acquired when the x-ray source is rotated about the fulcrum over a limited angular range. DTM slices reconstructed from the serial of PVs can provide quasi-3D structural information of the breast which may improve the conspicuity of breast cancer and also reduce the effects of the overlapping dense tissues.

In conventional mammography, computer-aided detection system (CADe) can increase the breast cancer detection rate by radiologists both in the laboratory and in clinical practice[2-7]. We are developing a CADe system to assist radiologists in detecting breast masses in DTMs. In this preliminary study, our purpose is to design an effective classifier to distinguish breast masses from normal tissues for false positive (FP) reduction in computerized mass detection in DTMs.

* jvwei@umich.edu, phone: 734-647-8553, Med-Inn Building C478, 1500 E. Medical Center Dr., Ann Arbor, MI 48109-5842

Medical Imaging 2008: Computer-Aided Diagnosis, edited by Maryellen L. Giger, Nico Karssemeijer
Proc. of SPIE Vol. 6915, 691508, (2008) · 1605-7422/08/$18 · doi: 10.1117/12.771189

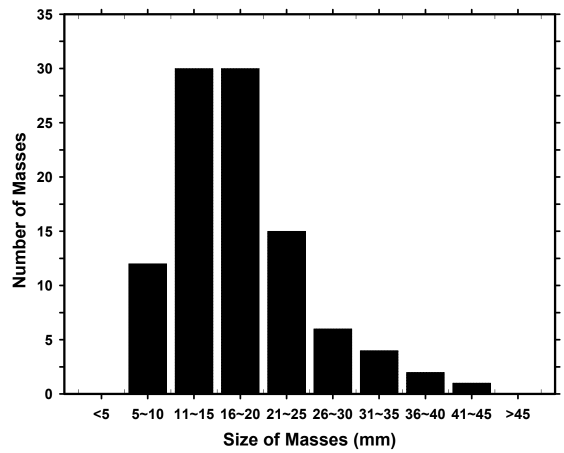

Figure 1. Histogram of the mass sizes measured on the central slices of the reconstructed DTMs. Mass sizes are measured as the longest dimension of the mass by an experienced MQSA radiologist. The size of the masses in this data set ranged from 5.5 mm to 43.4 mm with a mean size of 17.4±7.3 mm.

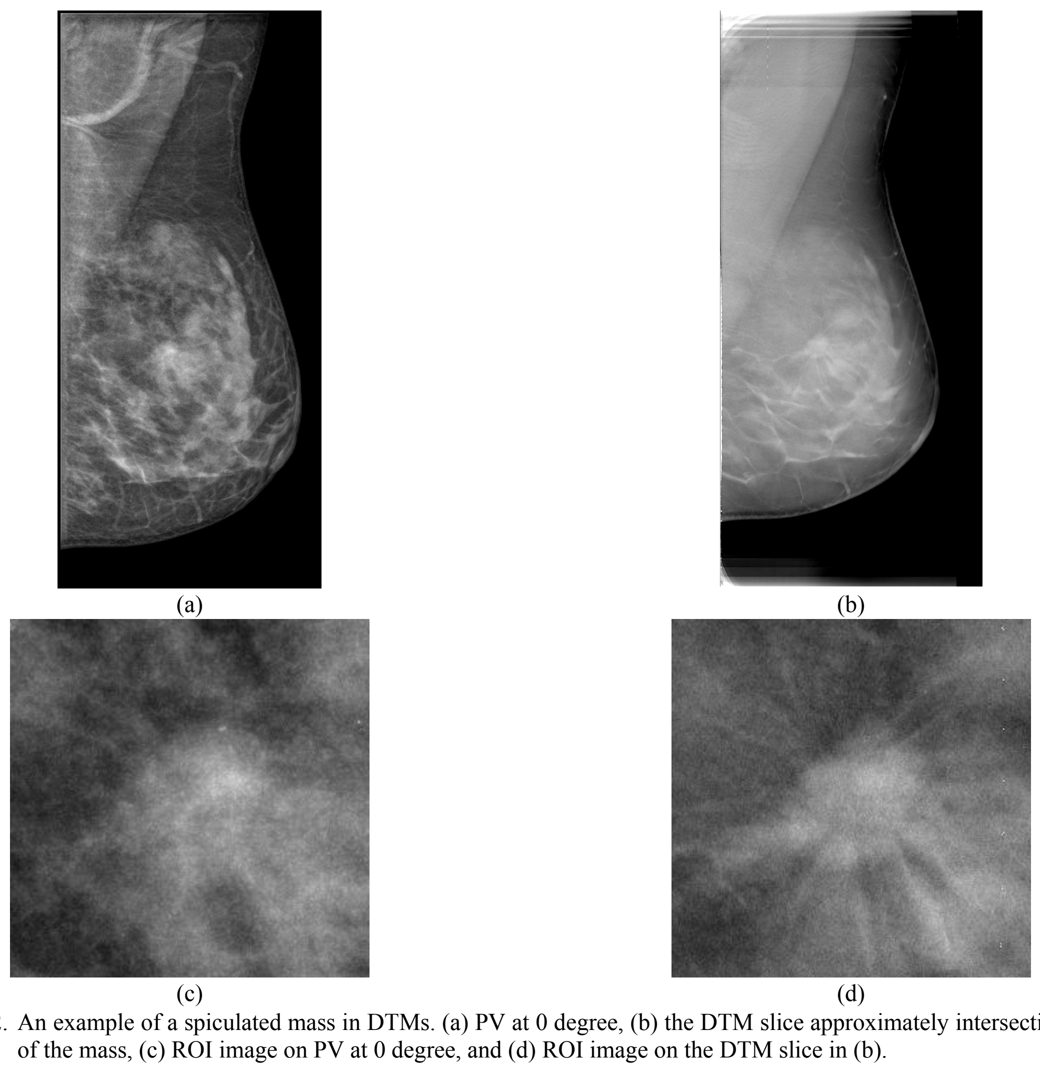

Figure 2. An example of a spiculated mass in DTMs. (a) PV at 0 degree, (b) the DTM slice approximately intersecting the center of the mass, (c) ROI image on PV at 0 degree, and (d) ROI image on the DTM slice in (b).

2. MATERIALS AND METHODS

2.1 Materials

DTMs in this study were collected with Institutional Review Board (IRB) approval in the Breast Imaging Research Laboratory at the Massachusetts General Hospital with a GE first generation prototype DTM system. The DTM system has a flat panel detector with a pixel size of 0.1 mm x 0.1 mm. It acquired 11 PVs in 5-degree increments over a total tomosynthesis angle of 50-degree. The total dose for the 11 PVs was designed to be less than 1.5 times that of a single conventional mammogram. Only mediolateral oblique view (MLO) DTM is collected for each case. The data set we used in this study contained 100 cases. Each case had one single breast DTM which was reconstructed by a simultaneous algebraic reconstruction technique (SART) developed in previous study[8]. SART method iteratively updates the imaged volume using each PV image sequentially. The number of reconstructed slices in this data set ranged from 45 to 90 depending on the compressed breast thickness. An experienced MQSA radiologist identified the location of the masses in the reconstructed DTM slices. There were 69 malignant and 31 benign masses in this data set including some large-area architectural distortions. Figures 1 showed the histograms of mass sizes measured on the central slices. The mass size ranged from 5.5 to 43.4 mm with a mean size of 17.4±7.3 mm on the central DTM slices. Figure 2 is an example of a DTM with a spiculated mass; the PV at 0 degree and the SART reconstructed slice approximately intersecting the center of the mass are shown.

2.2 Methods

2.2.1 CADe System Overview

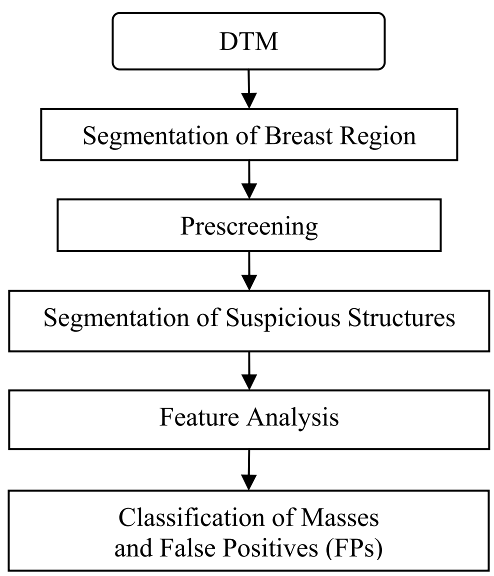

Figure 3. Block diagram of the CADe system for mass detection on DTMs.

Our CADe system consists of five processing steps: 1) segmentation of breast region on each reconstructed slice, 2) pre-screening of mass candidates, 3) identification of suspicious objects, 4) extraction of morphological and texture features, and 5) classification between the normal tissue and the mass regions by using LDA classifiers. The block diagram for the CADe system is shown in Figure 3.

We have described a prototype CADe system for detection of masses in the reconstructed DTM volumes previously.[9] For each reconstructed slice, the CADe system first segments the breast region from the background by using a breast boundary detection algorithm. The rest of the processes is only applied to the segmented breast region. For the pre-screening stage, we designed a 3D filter using the information of gradient field directions to identify mass candidates. After this enhancement filtering, the local maxima within the breast region were identified as the mass candidates on each DTM volume. Volumes of interest (VOI) were then identified in the breast with the center of a VOI placed at each of the mass candidates. The suspicious structure in each identified location was extracted by a 3D region growing method.

During the feature analysis and classification step, we evaluated three approaches to distinguish breast masses from normal tissues. In the first approach, referred to as 3D approach, we extracted morphological and run-length statistics texture features from the DTM slices. A linear discriminant analysis (LDA) classifier with stepwise feature selection was then trained to merge the useful features. In the second approach, referred to as 2D approach, the raw input PVs were first preprocessed with a Laplacian pyramid multiresolution enhancement scheme. A mass candidate was then forward-projected onto the each of the 11 PVs in order to determine the corresponding regions of interest (ROIs) on the preprocessed PVs. Spatial gray-level dependence (SGLD) texture features were extracted from each ROI and averaged over the 11 PVs. An LDA classifier with stepwise feature selection was designed to distinguish the masses from normal tissues. In the third approach, referred to as the combined approach, the LDA scores of a detected object, which represented the likelihood of the object being a mass, from the first and second approaches were merged to generate a combined mass likelihood score for each mass candidate. In this study, a simple averaging method was used to merge the information.

2.2.2 Training and test CADe system

The leave-one-case out re-sampling method was used for training and testing the FP classifiers. During training, feature selection with stepwise LDA was employed to obtain the best feature subset and reduce the dimensionality of the feature space to design an effective classifier. Briefly, for a data set of n cases, all mass candidates from a test case are left out while the other (n-1) cases are used for selection of predictor variables from the feature pool and estimation of the LDA classifier weights in each leave-one-case-out cycle. Since the appropriate threshold values for feature entry, feature elimination, and tolerance of feature correlation were unknown, we used an automated simplex optimization method to search for the best combination of thresholds in the parameter space. The trained LDA classifier was then applied to the mass candidates in the left-out case to obtain the mass likelihood score of each candidate. This process was performed with each of the n cases left out in turn so that all objects would be assigned a mass likelihood score at the completion of the n cycles.

2.2.3 Evaluation methods

In order to compare the performance of the three feature analysis and classification methods, we employed the receiver operating characteristic (ROC) analysis. The ROCKIT curve fitting software and statistical significance test for ROC analysis developed by Metz et al.[10] is used in this study. The discriminant scores from the three different approaches were input as the decision variable in the ROCKIT program, which fits a binormal ROC curve based on maximum likelihood estimation.

3. EXPERIMENTAL RESULTS

Figure 4 shows the test ROC curves for classification of breast masses and normal tissues on DTMs. The areas under the ROC curves (A_z) were 0.87±0.02, 0.86±0.02 and 0.91±0.02 for the 3D, 2D, and combined approaches, respectively. The difference between the A_z values of the 3D and 2D approaches did not achieve statistical significance (*p=0.50)*. The performance of the combined approach was significantly better than either the 3D or the 2D approach (*p=0.04 and p=0.03*, respectively*)*. Table 1 summarized the ROC results.

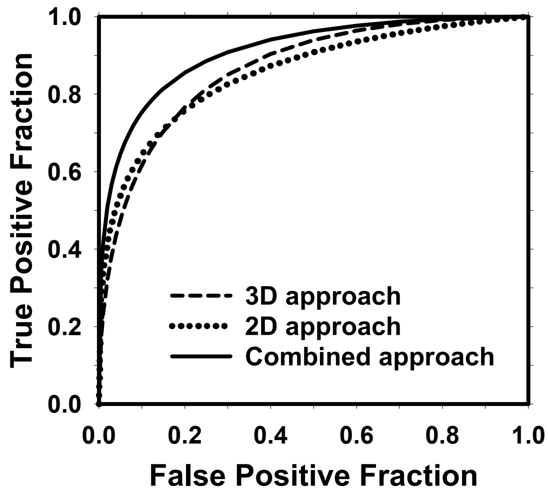

Figure 4. The test ROC curves for classification of breast masses from normal tissues on digital tomosynthesis mammography (DTM). The A_z values are 0.87±0.02, 0.86±0.02 and 0.91±0.02 for the 3D, 2D and combined approaches, respectively.

Table 1. Estimation of the statistical significance in the difference between the ROC performances of three feature analysis and classification approaches. A: 3D approach, B: 2D approach, C: combined approach.

	Az Value		P Value
A	0.87	A vs B	= 0.5
B	0.86	B vs C	< 0.05
C	0.91	C vs A	< 0.05

4. DISCUSSION AND CONCLUSIONS

In mammography, 3D anatomical structures are projected onto a 2D image plane, and the overlapping fibroglandular breast tissues reduce the visibility of breast cancer. DTM is one of the promising methods that provide quasi-3D structural information and may improve the sensitivity and specificity of breast cancer detection. In this study, we compared three methods for classification of breast masses and normal tissues in DTMs. The forward projection for extraction of 2D image information from the PVs is a new method for identifying corresponding ROIs for the detected objects. The combined approach which fuses the information on both the 2D projection views and 3D reconstructed slices is a promising approach to improving the differentiation of breast masses from normal tissues on DTMs. It is expected that the classifier will be useful for FP reduction in a computerized mass detection system.

ACKNOWLEGMENTS

This work is supported by USPHS grants CA120234 and CA95153, U. S. Army Medical Research and Materiel Command grants DAMD 17-02-1-0214, W81XWH-04-1-0475 and W81XXH-07-1-0324. The content of this paper does not necessarily reflect the position of the funding agencies and no official endorsement of any equipment and product of any companies mentioned should be inferred. The authors are grateful to Charles E. Metz, Ph.D., for the LABROC and ROCKIT programs.

REFERENCES

[1] "Cancer statistics 2006 presentation, www.Cancer.org" American Cancer Society (2006).

[2] Chan, H. P., Doi, K., Vyborny, C. J., Schmidt, R. A., Metz, C. E., Lam, K. L., Ogura, T., Wu, Y. and MacMahon, H., "Improvement in radiologists' detection of clustered microcalcifications on mammograms. The potential of computer-aided diagnosis," Investigative Radiology 25, 1102-1110 (1990).

[3] Warren Burhenne, L. J., Wood, S. A., D'orsi, C. J., Feig, S. A., Kopans, D. B., O'Shaughnessy, K. F., Sickles, E. A., Tabar, L., Vyborny, C. J. and Castellino, R. A., "Potential contribution of computer-aided detection to the sensitivity of screening mammography," Radiology 215, 554-562 (2000).

[4] Freer, T. W. and Ulissey, M. J., "Screening mammography with computer-aided detection: Prospective study of 12,860 patients in a community breast center," Radiology 220, 781-786 (2001).

[5] Brem, R. F., Baum, J. K., Lechner, M., Kaplan, S., Souders, S., Naul, L. G. and Hoffmeister, J., "Improvement in sensitivity of screening mammography with computer-aided detection: A multi-institutional trial," Am J Roentgenology 181, 687-693 (2003).

[6] Destounis, S. V., Dinitto, P., Logan-Young, W., Bonaccio, E., Zuley, M. L. and Willison, K. M., "Can computer-aided detection with double reading of screening mammograms help decrease the false-negative rate? Initial experience," Radiology 232, 578-584 (2004).

[7] Helvie, M. A., Hadjiiski, L. M., Makariou, E., Chan, H. P., Petrick, N., Sahiner, B., Lo, S. C. B., Freedman, M., Adler, D., Bailey, J., Blane, C., Hoff, D., Hunt, K., Joynt, L., Klein, K., Paramagul, C., Patterson, S. and Roubidoux, M. A., "Sensitivity of noncommercial computer-aided detection system for mammographic breast cancer detection - a pilot clinical trial," Radiology 231, 208-214 (2004).

[8] Zhang, Y., Chan, H. P., Sahiner, B., Wei, J., Goodsitt, M. M., Hadjiiski, L. M., Ge, J. and Zhou, C., "A comparative study of limited-angle cone-beam reconstruction methods for breast tomosynthesis," Medical Physics 33, 3781-3795 (2006).

[9] Chan, H. P., Wei, J., Sahiner, B., Rafferty, E. A., Wu, T., Roubidoux, M. A., Moore, R. H., Kopans, D. B., Hadjiiski, L. M. and Helvie, M. A., "Computer-aided detection system for breast masses on digital tomosynthesis mammograms - preliminary experience," Radiology 237, 1075-1080 (2005).

[10] Metz, C. E., "ROC methodology in radiologic imaging," Investigative Radiology 21, 720-733 (1986).

Digital tomosynthesis mammography: Improvement of artifact reduction method for high-attenuation objects on reconstructed slices

Jun Ge*, Heang-Ping Chan, Berkman Sahiner, Yiheng Zhang, Jun Wei,
Lubomir M. Hadjiiski, Chuan Zhou, Yi-Ta Wu, Jiazheng Shi

Department of Radiology, University of Michigan, Ann Arbor

ABSTRACT

One major image quality problem in digital tomosynthesis mammography (DTM) is the poor depth-resolution caused by the inherent incomplete sampling. This problem is more pronounced if high-attenuation objects, such as metallic markers and dense calcifications, are present in the breast. Strong ghosting artifacts will be generated in the depth direction in the reconstructed volume. Incomplete sampling of DTM can also cause visible ghosting artifacts in the x-ray source motion direction on the off-focus planes of the objects. These artifacts may interfere with radiologists' visual assessment and computerized analysis of subtle mammographic features. We previously developed an artifact reduction method by using 3D geometrical information of the objects estimated from the reconstructed slices. In this study, we examined the effect of imaging system blur in DTM caused by the focal spot and the detector modulation transformation function (MTF). The focal spot was simulated as a 0.3 mm square array of x-ray point sources. The detector MTF was simulated using the Burgess model with parameters derived from published data of a GE FFDM detector. The spatial-variant impulse responses for the DTM imaging system, which are required in our artifact reduction method, were then computed from the DTM imaging model and a given reconstruction technique. Our results demonstrated that inclusion of imaging system blur improved the performance of our artifact reduction method in terms of the visual quality of the corrected objects. The detector MTF had stronger effects than focal spot blur on artifact reduction under the imaging geometry used. Further work is underway to investigate the effects from other DTM imaging parameters, such as x-ray scattering, different polyenergetic x-ray spectra, and different configurations of angular range and angular sampling interval.

Keywords: Digital tomosynthesis mammography, tomographic reconstruction, artifact reduction, constrained iterative method, imaging system blur

1. INTRODUCTION

Digital tomosynthesis mammography[1, 2] (DTM) capitalizes on the strengths and proven abilities of conventional mammography, while providing the much-needed three-dimensional (3D) information. Display of the tomosynthesized breast volume with each reconstructed slice in sharp focus enhances lesion visibility and facilitates analysis of lesion margins by reducing overlapping structures in the breast volume. This may allow the radiologist to not only reduce missed cancers, but also make more accurate diagnoses of breast lesions. One major image quality problem in DTM is the poor depth resolution caused by the inherent incomplete sampling. This problem is more pronounced if high-attenuation objects, such as metallic markers and dense calcifications, are present in the breast. Strong ghosting artifacts will be generated in the depth direction in the reconstructed volume. Incomplete sampling of DTM can also cause visible ghosting artifacts in the x-ray source motion direction on the off-focus planes of the objects. These artifacts may interfere with radiologists' visual assessment and computerized analysis of subtle mammographic features.

A number of methods[3-8] have been proposed to suppress artifacts and enhance image quality for tomosynthesis. We previously developed a ghosting artifact reduction method by using 3D geometrical information of the objects estimated from the reconstructed slices[9]. The idea is based on the observation that high-attenuation objects in breasts being imaged are typically embedded in a local soft-tissue background that can be assumed to be quasi-homogeneous within the small local volume of interest (VOI). A set of linear equations can be used to describe the imaging process

* gejun@med.umich.edu, phone: 734-647-8556, Med Inn Building C474, 1500 E. Medical Center Dr., Ann Arbor, MI 48109-5842

Medical Imaging 2008: Physics of Medical Imaging, edited by Jiang Hsieh, Ehsan Samei,
Proc. of SPIE Vol. 6913, 69134O, (2008) · 1605-7422/08/$18 · doi: 10.1117/12.771539

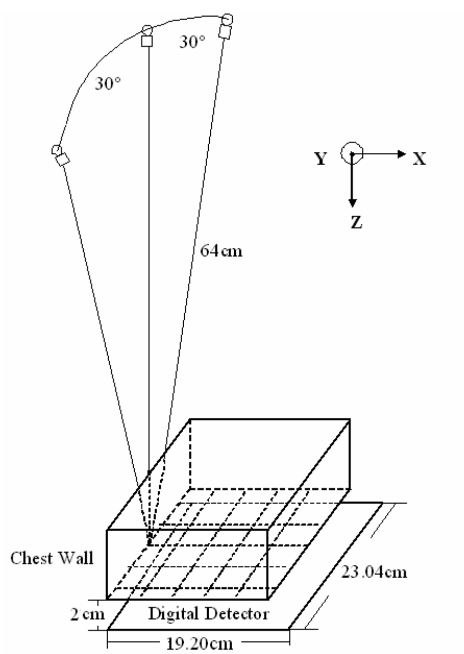
30°
30°
Y
X
Z
64cm
Chest Wall
23.04cm
2 cm
Digital Detector
19.20cm

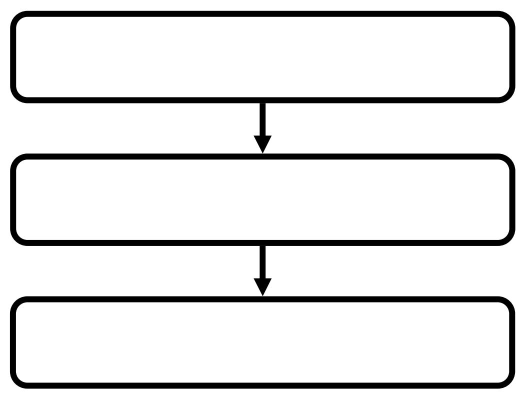

map. The prescreening process of an automated calcification detection system[10] for full-field digital mammograms (FFDMs) previously developed in our laboratory was used for the purpose. In order to find the 3D location and an approximate volume of the high-attenuation objects from the 2D segmentation on PVs, a simple voting scheme was used. In this scheme, each of the voxels in the 3D volume (0.1 mm isotropic voxel size) obtains one vote from a PV if a ray connecting the source and a non-zero pixel on the 2D binary map for this PV passes through the voxel. Thus each of the voxels in the 3D volume contained the number of the votes out of the 21 PV binary maps. A threshold of 14 was empirically chosen for this voting scheme. The connected voxels with values above 14 were segmented and identified as belonging to the same object. The center-of-mass of each segmented 3D object was defined as the object center. The bounding box for each 3D object was extended by 3 pixels (0.3 mm) on each side on the x-y plane to define the volume of interest (VOI) Ω for this object. If the neighboring VOIs overlapped, the two objects would be considered as one and the VOI would be extended to enclose both objects. Figure 3 shows the flowchart of the steps in this stage.

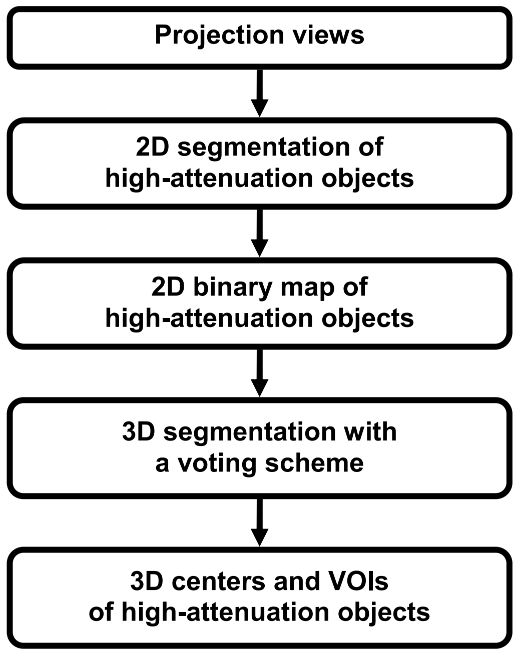

Fig. 3. Flowchart of the estimation of 3D geometrical information of the high-attenuation objects.

At the second stage, the VOI Ω containing each high-attenuation object is modeled as a homogeneous background with a high-attenuation object. The eLAC for a voxel within Ω is denoted as $x_p, p \in \Omega$. The eLAC is the sum of two parts, namely, the slow-varying background v_p and the contrast d_p. We assume the VOI Ω is isolated in the sense that the artifacts outside Ω caused by the high eLACs within Ω are small enough to be ignored. The projection-reconstruction (PR) system within Ω is then characterized by a set of linear equations $\hat{\mathbf{x}} - \hat{x}_n = \mathbf{C}_\Omega \mathbf{d}$, where $\hat{\mathbf{x}}$ is the vector of the voxel values $\hat{x}_p$ at p within Ω on the reconstruction slices, $\hat{x}_n$ is the average of the neighboring voxel values of the high-attenuation object to approximate the slow-varying part of $\hat{x}_p$, $\mathbf{C}_\Omega$ is the shift-variant 3D impulse response matrix for the PR system within Ω, and $\mathbf{d}$ is the vector of d_p's. Since $\mathbf{C}_\Omega$ is generally sparse and singular for DTM, direct matrix inversion is time-consuming and sensitive to the noise. Therefore, a constrained iterative method[11] was used to estimate the contrast eLAC value d_p's. The 3D segmentation of the high-attenuation object obtained at the previous stage was used as the initialization in this iterative method. The positivity of the eLACs was used as the constraint. Finally, the interplane artifacts are calculated as a linear combination of the impulse responses corresponding to each of the voxels of the high-attenuation objects and subtracted from the original reconstructed slices. For the voxels associated with the high-attenuation objects, the voxel values were replaced with the sum of the estimated background part and the contrast part: $\hat{x}_n + \hat{d}_p$.

3. MODELING OF DTM IMAGING SYSTEM BLUR

There are a number of sources of blur in X-ray imaging systems. In this study, we examined the effects of imaging blur in DTM system caused by the focal spot and the detector modulation transformation function (MTF). The real x-ray source is not a perfect point source. We divided it into elements that were small enough such that we can approximate its response by a point. We modeled the focal spot as a 0.3 mm array (3 by 3) of point x-ray sources to simulate the focal spot blur. The photon fluence was distributed to each simulated point x-ray source uniformly. The detector MTF was simulated using the Burgess model[12] with parameters derived from published data of a GE FFDM detector[13]. The Burgess model is given by $MTF(u) = 0.5erfc[\alpha \ln(u / u_0)]$, where u is the spatial frequency and $erfc[\cdot]$ is the complementary error function[12]. The two adjustable parameters α and u_0 were estimated as 0.71 and 2.92, respectively, by curve fitting. The MTF data of the GE FFDM detector[13] and the MTF curve fitted with Burgess Model[12] are shown in Fig. 4. The fitted MTF is then applied to the calculation of the shift-variant 3D impulse response matrix $\mathbf{C}_\Omega$ for the PR system within Ω.

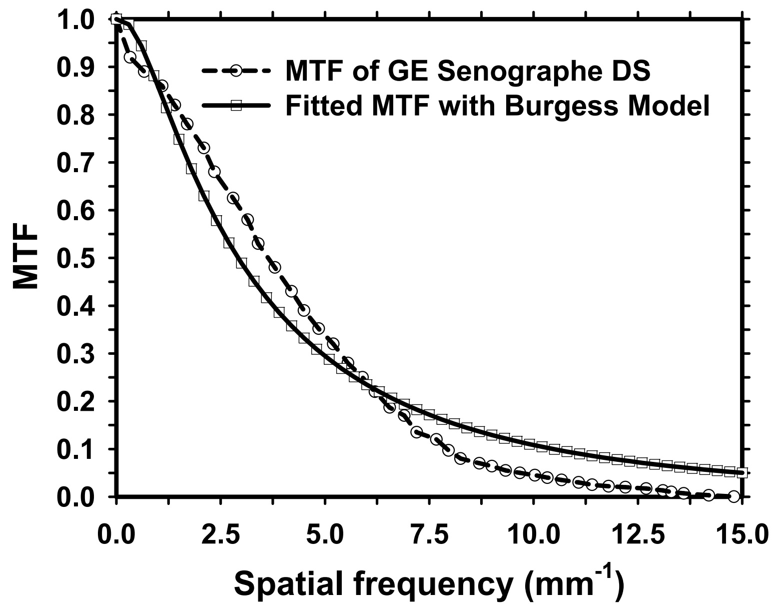

Fig. 4. MTF of GE Senographe DS system (dashed line) and the MTF fitted with Burgess Model (solid line).

4. RESULTS

A patient DTM with a large dense calcification was selected from our collected DTM database to evaluate the performance of artifact reduction. A simulated high-attenuation object with preset eLACs that approximately match the attenuation of calcifications were digitally generated and projected onto the PVs near the real dense calcification of the patient DTM. DTM slices were then reconstructed from the PVs and processed with our artifact reduction method as described in Section 3. The artifact reduction performance for the simulated high-attenuation object was compared to that of the real calcification in the artifact-reduced DTMs. This artifact correction process was performed both with and without taking into consideration the system blur.

The artifact reduction results in Fig. 5 shows that the inclusion of imaging system blur resulted in improved artifact-reduced images for both the simulated and real objects. The corrected objects are not as artificially sharp and bright as the images obtained from the correction without considering the system blur. Some internal features of the real

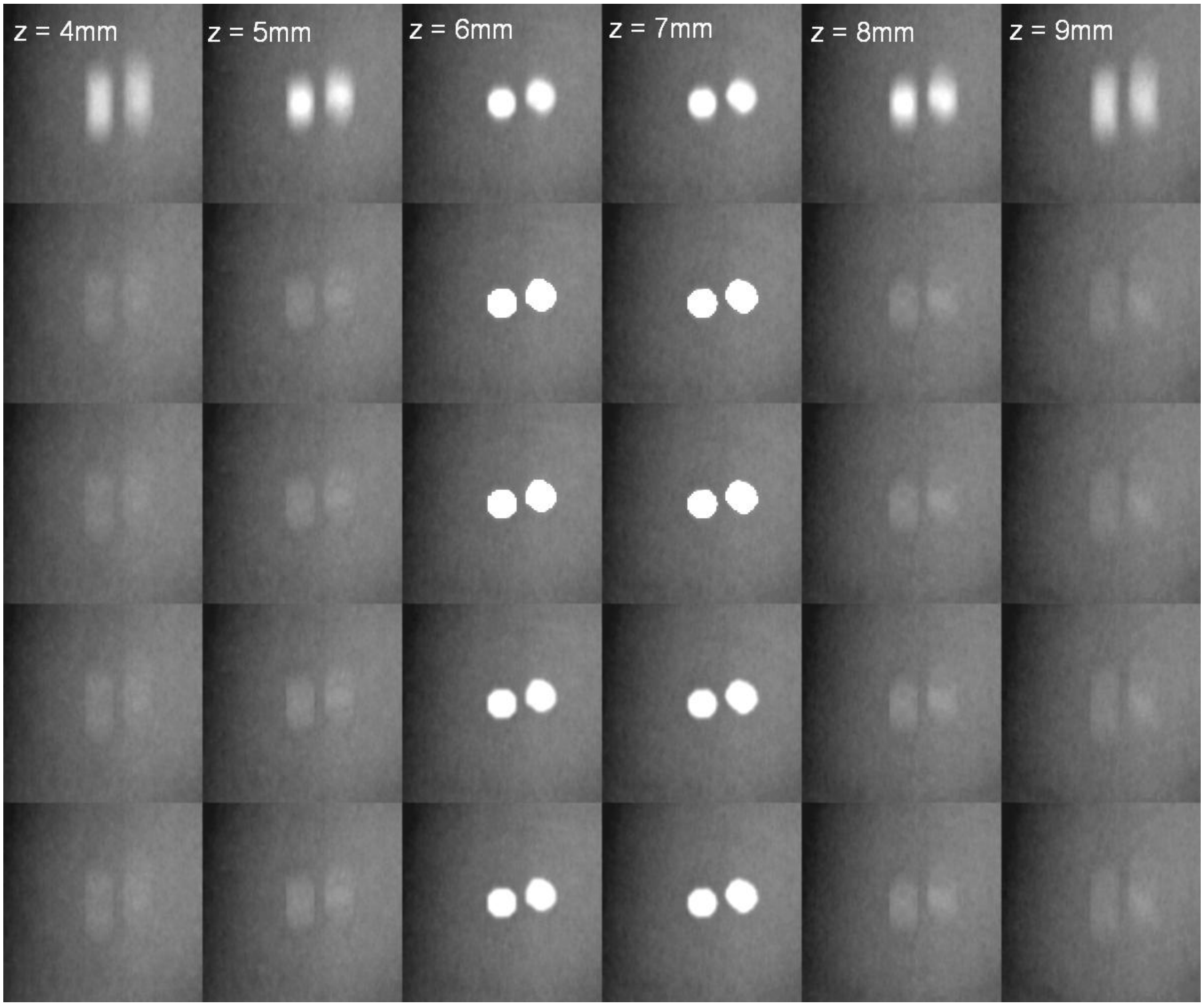
z = 4mm
z = 5mm
z = 6mm
z = 7mm
z = 8mm
z = 9mm

ACKNOWLEDGMENTS

This work is supported by USPHS grants CA120234, CA95153, and U. S. Army Medical Research and Materiel Command grant W81XWH 07-1-0324. The content of this paper does not necessarily reflect the position of the funding agency and no official endorsement of any equipment and product of any companies mentioned should be inferred. The digital tomosynthesis system was developed by the GE Global Research Group through the Biomedical Research Partnership (USPHS grant CA91713) collaboration.

REFERENCES

[1] Niklason, L. T., Christian, B. T., Niklason, L. E., Kopans, D. B., Castleberry, D. E., Opsahl-Ong, B. H., Landberg, C. E., Slanetz, P. J., Giardino, A. A., Moore, R., Albagli, D., Dejule, M. C., Fitzgerald, F. C., Fobare, D. F., Giambattista, B. W., Kwasnick, R. F., Liu, J., Lubowski, S. J., Possin, G. E., Richotte, J. F., Wei, C. Y. and Wirth, R. F., "Digital tomosynthesis in breast imaging," Radiology 205, 399-406 (1997).

[2] Dobbins, J. T. and Godfrey, D. J., "Digital x-ray tomosynthesis: Current state of the art and clinical potential," Physics in Medicine and Biology 48, R65-R106 (2003).

[3] Chakraborty, D. P., Yester, M. V., Barnes, G. T. and Lakshminarayanan, A. V., "Selfmasking subtraction tomosynthesis," Radiology 150, 225-229 (1984).

[4] Sone, S., Kasuga, T., Sakai, F., Aoki, J., Izuno, I., Tanizaki, Y., Shigeta, H. and Shibata, K., "Development of a high-resolution digital tomosynthesis system and its clinical application," Radiographics 11, 807-822 (1991).

[5] Roy, D. N. G., Kruger, R. A., Yih, B. and Rio, P. D., "Selective plane removal in limited angle tomographic imaging," Medical Physics 12, 65-70 (1985).

[6] Ruttimann, U. E., Groenhuis, R. A. J. and Webber, R. L., "Restoration of digital multiplane tomosynthesis by a constrained iteration method," IEEE Transactions on Medical Imaging MI-3, 141-148 (1984).

[7] Godfrey, D. J., McAdams, H. P. and Dobbins, J. T., "Optimization of the matrix inversion tomosynthesis (MITS) impulse response and modulation transfer function characteristics for chest imaging," Medical Physics 33, 655-667 (2006).

[8] Wu, T., Moore, R. H. and Kopans, D. B., "Voting strategy for artifact reduction in digital breast tomosynthesis," Medical Physics 33, 2461-2471 (2006).

[9] Ge, J., Chan, H.-P., Sahiner, B., Zhang, Y., Wei, J., Hadjiiski, L. M. and Zhou, C., "Digital tomosynthesis mammography: Intra- and interplane artifact reduction for high-contrast objects on reconstructed slices using a priori 3d geometrical information," Proc. SPIE 6512, 4Q1-4Q8 (2007).

[10] Ge, J., Sahiner, B., Hadjiiski, L. M., Chan, H.-P., Wei, J., Helvie, M. A. and Zhou, C., "Computer aided detection of clusters of microcalcifications on full field digital mammograms," Medical Physics 33, 2975-2988 (2006).

[11] Schafer, R. W., Mersereau, R. M. and Richards, M. A., "Constrained iterative restoration algorithms," Proceedings of the IEEE 69, 432-451 (1981).

[12] Burgess, A. E., "An empirical equation for screen MTFs," Medical Physics 5, 199-204 (1978).

[13] Monnin, P., Gutierrez, D., Bulling, S., Guntern, D. and Verdun, F. R., "A comparison of the performance of digital mammography systems," Medical Physics 34, 906-914 (2007).

Digital tomosynthesis mammography: comparison of mass classification using 3D slices and 2D projection views

Heang-Ping Chan*, Yi-Ta Wu, Berkman Sahiner, Yiheng Zhang, Jun Wei, Richard H. Moore[a], Daniel B. Kopans[a], Mark A. Helvie, Lubomir Hadjiiski, Ted Way
Department of Radiology, University of Michigan, Ann Arbor, MI
[a]Department of Radiology, Massachusetts General Hospital, Boston, MA

ABSTRACT

We are developing computer-aided diagnosis (CADx) methods for classification of masses on digital breast tomosynthesis mammograms (DBTs). A DBT data set containing 107 masses (56 malignant and 51 benign) collected at the Massachusetts General Hospital was used. The DBTs were obtained with a GE prototype system which acquired 11 projection views (PVs) over a 50-degree arc. We reconstructed the DBTs at 1-mm slice interval using a simultaneous algebraic reconstruction technique. The regions of interest (ROIs) containing the masses in the DBT volume and the corresponding ROIs on the PVs were identified. The mass on each slice or each PV was segmented by an active contour model. Spiculation measures, texture features, and morphological features were extracted from the segmented mass. Four feature spaces were formed: (1) features from the central DBT slice, (2) average features from 5 DBT slices centered at the central slice, (3) features from the central PV, and (4) average features from all 11 PVs. In each feature space, a linear discriminant analysis classifier with stepwise feature selection was trained and tested using a two loop leave-one-case-out procedure. The test Az of 0.91±0.03 from the 5-DBT-slice feature space was significantly ($p=0.003$) higher than that of 0.84±0.04 from the 1-DBT-slice feature space. The test Az of 0.83±0.04 from the 11-PV feature space was not significantly different ($p=0.18$) from that of 0.79±0.04 from the 1-PV feature space. The classification accuracy in the 5-DBT-slice feature space was significantly better ($p=0.006$) than that in the 11-PV feature space. The results demonstrate that the features of breast lesions extracted from the DBT slices may provide higher classification accuracy than those from the PV images.

Keywords: Digital breast tomosynthesis, computer-aided classification, masses, SART

1. INTRODUCTION

In mammography, the presence of overlapping dense fibroglandular tissue reduces the conspicuity of the abnormalities, making it difficult to detect or to characterize a lesion. This problem may be alleviated by digital breast tomosynthesis mammography (DBT). In DBT, a series of projection view (PV) images is acquired as the x-ray source is rotated over a limited range of angles. The total dose required for DBT is kept at nearly the same or only slightly higher than that of a regular mammogram. Tomographic slices of the imaged volume can be generated with reconstruction techniques from the series of PV images. The DBT slices provide quasi-3D structural information and may reduce the camouflaging effects of fibroglandular tissues. DBT is one of the promising methods that may improve the detection and characterization for breast lesions.[1]

Computer-aided detection (CADe) and computer-aided diagnosis (CADx) have been shown to improve breast cancer detection and characterization in mammography. It is expected that computer-aided image analysis will play a role in DBT because of the large number of images that need to be interpreted. Efforts are underway to develop computerized detection systems for DBT.[2-8] We have previously investigated the feasibility of developing a CADx system for breast masses using the reconstructed DBT slices as input.[9] The purpose of the current study is to evaluate an alternative approach of using the 2D PV images as input, and compare its performance with that of the approach of using the DBT slices as input.

*e-mail: chanhp@umich.edu

Medical Imaging 2008: Computer-Aided Diagnosis, edited by Maryellen L. Giger, Nico Karssemeijer
Proc. of SPIE Vol. 6915, 691506, (2008) · 1605-7422/08/$18 · doi: 10.1117/12.770422

2. MATERIALS AND METHODS

2.1 Data Set

A data set of 107 masses (56 malignant and 51 benign) was used in this study. The DBTs were acquired with a GE prototype system at the Massachusetts General Hospital with IRB approval. The DBT system acquired 11 PVs in 5-degree increments over an arc of 50 degrees. The breasts were imaged in the mediolateral oblique (MLO) view. We reconstructed the DBTs at 1-mm slice interval using a simultaneous algebraic reconstruction technique (SART). The volume of interest (VOI) containing the mass was identified by a Mammography Quality Standards Act (MQSA)-approved radiologist on each DBT volume. The VOI was marked as a rectangular region of interest (ROI) on the approximately central slice where the mass was best visualized, and bounded from the top and the bottom by the first and the last slice where the mass became almost invisible. The mass ROI was extracted from each DBT slice with a margin of about 4 mm around the bounding box. For a given mass, the corresponding ROIs on the PVs were located by forward projection of the central slice of the mass to the PVs using the known geometry of the DBT system. The longest diameter of the mass on the central DBT slice was estimated by the radiologist using an electronic caliper.

2.2 Feature Extraction

The automated mass classification scheme used for analysis of both DBT slices and PV images in this study is shown in Fig. 1. The mass ROI from an individual image is used as input. The mass is segmented from its breast tissue background. Three types of image features, namely, spiculation, texture, and morphological features are extracted from the segmented mass to describe the size, shape, margin characteristics, and texture in the breast tissue surrounding the mass. For mass classification using multiple images, the corresponding features extracted from the different images are averaged. To reduce the dimensionality of the feature space, stepwise feature selection is performed to identify the most effective features. A feature classifier is then designed for the differentiation of malignant and benign masses in the multi-dimensional feature space.

For an input ROI image from a DBT slice or a PV image, the mass is segmented by an active contour model initialized with adaptive k-means clustering followed by morphological filtering. For extraction of spiculation features, a spiculation likelihood map is generated by analyzing the gradient directions around the mass margin and spiculation measures are extracted from the map.[10] For extraction of texture features in tissues around the mass, the rubber band straightening transform (RBST) is applied to a band of pixels around the segmented mass boundary such that the mass boundary was in the horizontal direction and the spiculations are approximately in the vertical direction.[11] The gradient of the RBST image is enhanced by Sobel filtering in both the horizontal and vertical directions. The run-length statistics (RLS) texture features are then extracted from the gradient images. Morphological features including the mass size, the Fourier descriptor, and those from the normalized radial length (NRL) are extracted to describe the mass shape and size.

For analysis using the reconstructed DBT slices, we compared a feature space obtained from features of the central slice alone and a second feature space obtained by averaging the corresponding features from 5 slices centered at the central slice. For classification of the masses using the PVs, we evaluated a feature space obtained from the central PV alone and another by averaging the corresponding features from all 11 PVs.

2.3 Feature Classification

In each feature space, a linear discriminant analysis (LDA) classifier with stepwise feature selection was trained and tested using a two-loop leave-one-case-out resampling procedure. In the "outer" leave-one-case-out loop, one case including all mass ROIs from the same patient was left out in each cycle. Simplex optimization was used to automatically select the best set of parameters for a stepwise feature selection procedure within the training set of (N-1) cases in that cycle. During the simplex optimization process, an "inner" leave-one-case-out loop was used to obtain an area (A_z) under the receiver operating characteristic (ROC) curve from the (N-1) validation cases as a figure-of-merit for guiding the search. The best set of parameters was then used to select features from the entire training set of (N-1) cases and an LDA classifier was formulated. The LDA was applied to the left-out case to obtain a test discriminant score. The same process was repeated for all N cases in the data set in the outer leave-one-case-out loop. After the two-loop resampling procedure was completed, the test scores for all N cases were collected and evaluated by ROC analysis. The classification accuracy of the classifier was estimated as the test A_z.

The same feature selection and classification procedure was performed in each of the feature spaces as shown in Fig. 1. The test ROC curves and the A_z values were then compared for the four conditions.

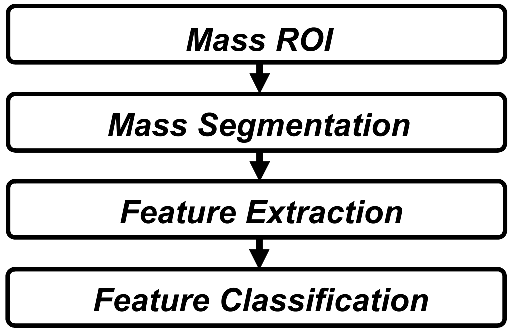

Fig. 1. Mass classification scheme for both approaches using the PVs as input and using the DBT slices as input.

3. RESULTS

An example of an ROI in the PV and the DBT of a breast with a spiculated mass is shown in Fig. 2. The ROIs from the PV at 0 degree and from a SART reconstructed slice through approximately the center of the mass are shown.

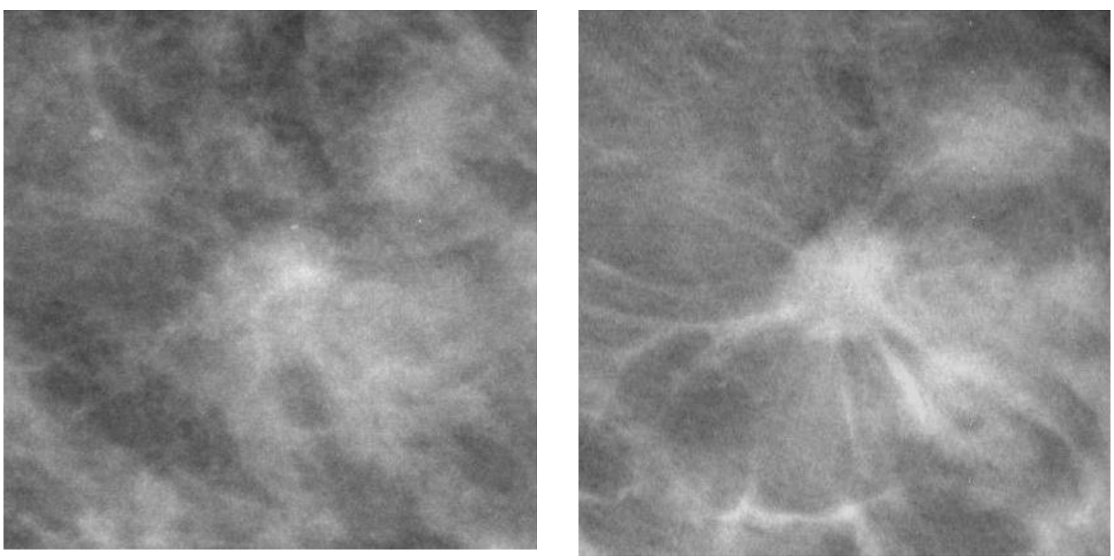

(a) (b)

Fig. 2. An example of a spiculated mass in the data set. (a) the ROI image in the central projection view (0 degree), and (b) the ROI from the SART-reconstructed slice intersecting approximately the center of the same mass. The spicules radiating from the mass can be seen much more clearly in the DBT slice.

The classification of masses using the reconstructed DBT slices achieved a test A_z of 0.84±0.04 and 0.91±0.03, respectively, in the central DBT slice feature space and in the 5-DBT-slice feature space. The difference in the A_z between the central DBT slice and 5-DBT-slice feature spaces was statistically significant (p=0.003). For classification of masses using the PVs, the test A_z was 0.79±0.04 and 0.83±0.04, respectively, in the central PV feature space and in the 11-PV feature space. The difference in the A_z between the central PV and 11-PV feature space did not achieve statistical significance (p=0.18). Finally, the classification accuracy in the 5- DBT-slice feature space was significantly better (p=0.006) than that in the 11-PV feature space. The A_z values are summarized in Table 1 and the ROC curves obtained under the four conditions are compared in Fig. 3.

Table 1. The classification performance of the LDA classifiers in the four feature spaces.

A_z (PV)	A_z (DBT)
Single PV: 0.79±0.04	Central slice: 0.84±0.04
11 PVs: 0.83±0.04	5 slices: 0.91±0.03

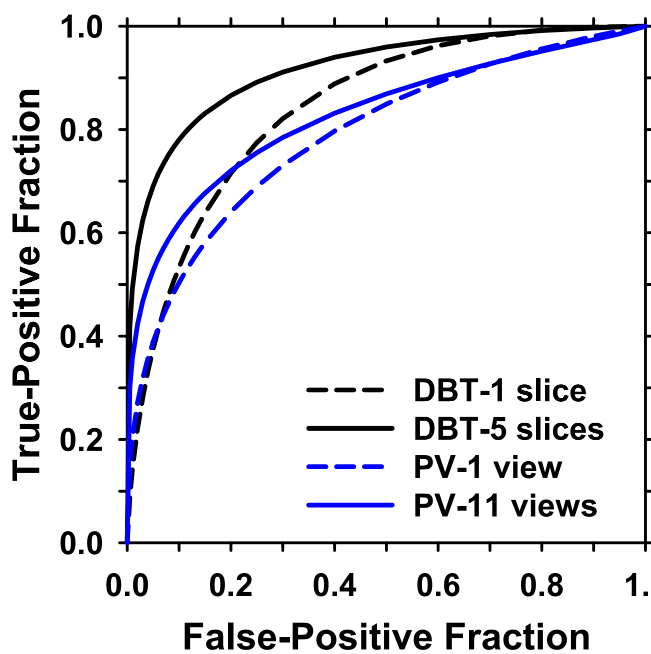

Fig. 3. ROC curves of the LDA classifiers in the four feature spaces: (1) features extracted from a single DBT slice intersecting approximately the center of the mass, (2) features extracted from 5 DBT slices centered at the central slice and averaged, (3) features extracted from a single PV image at the center of the tomosynthesis scan (0 degree projection angle), and (4) features extracted from 11 PVs centered at the 0 degree PV and averaged.

4. DISCUSSION AND CONCLUSIONS

DBT is a new imaging modality that holds the promise of improving breast cancer diagnosis by reducing the overlapping dense tissue that may obscure the characteristics of mass margins. Development of CAD systems for DBT is still at an early stage. In this preliminary study, we compared the effectiveness of the mass characteristics obtained by computerized feature analysis on the reconstructed DBT slices and on the PV images to differentiate malignant and benign masses. To our knowledge, this is the first study that compared mass classification in DBT using the two different approaches.

Our results demonstrate that the features of breast lesions extracted from DBT slices could provide significantly higher accuracy than those from PV images for classification of malignant and benign masses. Furthermore, the feature spaces obtained by averaging corresponding features from several DBT slices or from the PVs could provide significantly higher accuracy than those from the central slice or from the central PV alone, respectively. Although all image information is already contained in the set of PV images, tomosynthesis reconstruction can combine the information from the multiple PVs more efficiently than simply averaging the features extracted from the individual PVs. This results in the higher classification accuracy achieved using features from the DBT slices than using features from the PVs. For a given approach, the average features from multiple PVs or DBT slices provided a higher accuracy than features from a single image probably because of noise reduction. Study is underway to further improve both approaches and to evaluate the effects of combining the feature spaces. A larger data set is also being collected to improve the training of the CADx systems.

ACKNOWLEDGMENTS

This work is supported by USPHS grants CA120234 and CA95153, and U. S. Army Medical Research and Materiel Command grant DAMD 17-02-1-0214. The content of this paper does not necessarily reflect the position of the funding agencies and no official endorsement of any equipment and product of any companies mentioned should be inferred.

REFERENCES

[1] Helvie, M. A., Roubidoux, M. A., Hadjiiski, L. M., Zhang, Y., Carson, P. L. and Chan, H.-P., "Tomosynthesis mammography vs conventional mammography: Comparison of breast masses detection and characterization," RSNA Program Book 2007, 381 (2007).

[2] Chan, H. P., Wei, J., Sahiner, B., Rafferty, E. A., Wu, T., Ge, J., Roubidoux, M. A., Moore, R. H., Kopans, D. B., Hadjiiski, L. M. and Helvie, M. A., "Computer-aided detection on digital breast tomosynthesis (DBT) mammograms - comparison of two approaches," RSNA Program Book 2004, 447 (2004).

[3] Reiser, I., Nishikawa, R. M., Giger, M. L., Wu, T., Rafferty, E., Moore, R. H. and Kopans, D. B., "Computerized detection of mass lesions in digital breast tomosynthesis images using two- and three dimensional radial gradient index segmentation," Technology in Cancer Research and Treatment 3, 437-441 (2004).

[4] Chan, H.-P., Wei, J., Sahiner, B., Rafferty, E. A., Wu, T., Roubidoux, M. A., Moore, R. H., Kopans, D. B., Hadjiiski, L. M. and Helvie, M. A., "Computer-aided detection system for breast masses on digital tomosynthesis mammograms - preliminary experience," Radiology 237, 1075-1080 (2005).

[5] Chan, H.-P., Wei, J., Wu, T., Sahiner, B., Rafferty, E. A., Hadjiiski, L. M., Helvie, M. A., Roubidoux, M. A., Moore, R. H. and Kopans, D. B., "Computer-aided detection on digital breast tomosynthesis (DBT) mammograms: Dependence on image quality of reconstruction," RSNA Program Book 2005, 269 (2005).

[6] Chan, H. P., Wei, J., Zhang, Y., Helvie, M. A., Moore, R. H., Kopans, D., Roubidoux, M. A., Sahiner, B. and Hadjiiski, L. M., "Digital breast tomosynthesis (DBT) mammography: Computer-aided mass detection by fusion of tomosynthesis and 3d mass likelihood information," RSNA Program Book 2006, 230 (2006).

[7] Reiser, I., Nishikawa, R. M., Giger, M. L., Wu, T., Rafferty, E. A., Moore, R. H. and Kopans, D. B., "Computerized mass detection for digital breast tomosynthesis directly from the projection images," Medical Physics 33, 482-491 (2006).

[8] Chan, H. P., Wei, J., Zhang, Y., Moore, R. H., Kopans, D. B., Hadjiiski, L. M., Sahiner, B., Roubidoux, M. A. and Helvie, M. A., "Computer-aided detection of masses in digital tomosynthesis mammography: Combination of 3D and 2D detection information," Proc. SPIE 6514, 161-166 (2007).

[9] Chan, H. P., Wu, Y. T., Sahiner, B., Zhang, Y., Moore, R. H., Kopans, D. B., Helvie, M. A., Hadjiiski, L. M. and Way, T., "Analysis of mass characteristics on digital breast yomosynthesis (DBT) mammograms: Application to computer-aided diagnosis," RSNA Program Book 2007, 315 (2007).

[10] Sahiner, B., Petrick, N., Chan, H. P., Hadjiiski, L. M., Paramagul, C., Helvie, M. A. and Gurcan, M. N., "Computer-aided characterization of mammographic masses: Accuracy of mass segmentation and its effects on characterization," IEEE Transactions on Medical Imaging 20, 1275-1284 (2001).

[11] Sahiner, B., Chan, H. P., Petrick, N., Helvie, M. A. and Goodsitt, M. M., "Computerized characterization of masses on mammograms: The rubber band straightening transform and texture analysis," Medical Physics 25, 516-526 (1998).

Investigation of Different PV Distributions in Digital Breast Tomosynthesis (DBT) Mammography

Yiheng Zhang[1], Heang-Ping Chan[1], Mitchell M. Goodsitt[1], Andrea Schmitz[2], Jeffrey W. Eberhard[2], and Bernhard E. H. Claus[2]

[1] Department of Radiology, University of Michigan, Ann Arbor, MI
[2] GE Global Research, Niskayuna, NY

Abstract. Digital Breast Tomosynthesis (DBT) Mammography is an emerging technique that has the potential to improve breast cancer detection. In DBT, low-dose mammograms are acquired at a number of projection angles over a limited range and the 3D breast volume is reconstructed. In this study, we investigated the effect of different distributions of projection-view (PV) images that included different angular range and angular spacing on the reconstruction image quality. A GE prototype DBT system was used to acquire a total of 21 PVs in 3º increments over a ±30º range, from which multiple subsets containing the same number of 11 PV images were selected. A custom-built breast phantom and a selected patient case were used to evaluate the image quality. For breast phantom study, the contrast-to-noise ratio (CNR), the normalized line profiles of test objects, and an artifact spread function (ASF) were used as performance measures to compare the results for the different subsets and for the full set. The simultaneous algebraic reconstruction technique (SART) was used to reconstruct the DBT under all conditions. Our results demonstrated that large DBT angular range gave superior CNR and ASF for masses and less interplane blurring for high-density objects. Narrow angular range favors in-plane edge sharpness for high-density objects.

Keywords: Digital Breast Tomosynthesis (DBT) Mammography, distributions of projection-view (PV) images, simultaneous algebraic reconstruction technique (SART).

1 Introduction

Digital breast tomosynthesis (DBT) mammography is an emerging technique that can provide volumetric information for the breast. The breast volume is reconstructed from multiple low-dose projection-view (PV) images acquired at a number of angles in a limited angular range [1,2]. The total radiation dose is set to be comparable to that used in regular mammography. The depth resolution obtained in DBT can reduce the camouflaging effect of the overlapping fibroglandular breast tissue in conventional mammography and improve the conspicuity of subtle lesions, and thus potentially improve breast cancer detection at its early stage [3,4].

Different from computerized tomography, DBT is a limited-angle imaging modality. The system design, including but not limited to the parameters such as the number of PVs, the total angular range and the angular spacing, needs systematic investigation. The reconstruction image quality depends strongly on the selection of these and other parameters and the reconstruction algorithm. In this work, our purpose is to investigate the effect of different distributions of PV images on the reconstructed image quality based on a fixed total dose. The results will provide insight into the design of DBT systems and information for optimizing imaging conditions.

2 Methods

2.1 DBT System

A GE GEN2 DBT Mammography system was used to acquire a total of 21 PVs in 3º increments over a ±30º range [5]. The imaging geometry of this DBT system is schematically shown in Figure 1. The distance from the x-ray focal spot to the center of rotation is 64 cm and the focal-spot-to-detector distance is 66 cm. The system has a CsI phosphor/a:Si active matrix flat panel digital detector with a pixel size of 0.1 mm×0.1 mm. The image acquisition process takes less than 8 seconds and the digital detector (X-Y plane) is stationary during image acquisition. The system is operated at an exposure level that acquires a DBT mammography at about 1.5 times of the dose of a conventional screen-film mammogram.

In a preliminary study [6], we demonstrated that the simultaneous algebraic reconstruction technique (SART) [7] can provide high-quality tomosynthesized slices while being more efficient than statistical reconstruction methods for specific system configurations and imaging conditions. In this study, we employed SART for DBT reconstruction. The imaged volume was subdivided into an array of voxels, of which the X and Y dimensions were set to be 0.1 mm, the same as the detector pixel size, and the Z dimension (slice interval or spacing) 1.0 mm. In SART, an update of the 3D volume of the attenuation properties of breast tissue was performed using individual PV sequentially.

2.2 Different PV Distributions

Among many factors, the distribution of PV angles plays an important role in DBT system design. The total angular range and the angular sampling interval directly affect the reconstruction image quality. For low-contrast objects such as masses, and high-contrast objects such as calcifications, the same PV distribution may have different influences on the detection and characterization.

To investigate the effect of the distribution of PV angles on DBT image quality, six subsets, each containing 11 PVs, were selected from the original 21 PVs. These six subsets fell into three categories, namely, uniform group, non-uniform central group, and non-uniform extreme group. The uniform group included two conditions, representing a narrow and a wide angular range, in which each PV was spaced in equal angular intervals. The two non-uniform groups also contained two conditions in

each: the central group had more PVs in the middle region while the extreme group had more PVs in the extreme side regions. The two conditions in each non-uniform group slightly differed in distribution. The total dose for each subset was equal because they contained the same number of PVs. In tomosynthesis reconstruction, it is known that PV images acquired close to the middle region are important for the spatial resolution on the X-Y plane, while those acquired close to the extreme side region are important for the depth resolution. The PV distributions in this study were chosen to evaluate the trade-off among those non-uniform distribution groups and the uniform groups.

The x-ray source positions in terms of projection angles for the six subsets are listed in Table 1 and schematically shown in Figure 2. The six subsets are referred to as *Uniform-Narrow* (UN), *Uniform-Wide* (UW), *Nonuniform-Central-Dense* (NCD), *Nonuniform-Central-Sparse* (NCS), *Nonuniform-Extreme-Dense* (NED), and *Nonuniform-Extreme-Sparse* (NES) sampling, respectively. The DBT reconstruction using all 21 PVs available is referred to as the *Full-Set* (FS). Two SART iterations were used in the reconstruction of all subset conditions, providing a total of 22 updates (the number of updates in one SART iteration is equal to the number of PVs used for reconstruction), which was approximately equivalent to that of one iteration when the full set was used. The relaxation parameters were set to be 0.5 and 0.3 for the two iterations based on a visual comparison of the reconstructed images of a patient case at different relaxation parameter combinations.

2.3 Breast Phantom and Figures of Merit

To quantitatively evaluate the reconstructed image quality, a custom-built breast phantom was used which contained test objects on a thin feature layer sandwiched between five 1-cm-thick homogeneous Lucite plates below and another 1-cm-thick plate above. The test objects included layers of thin circular aluminum foils to simulate masses with different contrasts and high-contrast metal wires to simulate metal markers. The wire was placed approximately perpendicular to the chest wall edge in order to evaluate the DBT blurring along the x-ray source moving direction which was parallel to the chest-wall edge. The contrast-to-noise ratio (CNR), the normalized line profiles of test objects, and an artifact spread function (ASF) were used as performance measures to compare the results of different subset conditions and that of using the full set. The CNR of a simulated mass was defined as the difference in the average pixel intensities between the mass and its local image background, divided by the standard deviation of pixel intensity in the same background. The ASF of the mass was defined as the ratio of the CNR values between a given off-focus layer and the feature layer, and the ROIs extracted for the calculation of CNR values on different layers were located in the same positions in terms of the X and Y coordinates. Thus, the ASF quantified the inter-plane artifacts along the Z-direction. The line profile of a mass was extracted from the pixel intensities along the scan direction of the x-ray source (Y-axis) with the removal of the mean pixel intensity. Similarly, to facilitate the comparison of relative sharpness, line profiles of the wires were extracted along both the Y and Z axes, and the resulting maximum intensity was normalized to 1 after removal of the mean pixel intensity.

3 Results

The CNR values of selected simulated masses with different contrasts were listed in Table 2 for all imaging conditions. The CNR values are sorted approximately in an ascending order with the corresponding total angular range, and the number of PVs outside ±6º is also listed in order to illustrate the sampling density in the extreme side regions. The results suggested that the mass CNR value depended primarily on the total angular range and to some extent on the number of PVs acquired at large projection angles. Among the six subsets, the UW and NED sampling that have more PVs in the extreme side regions and the largest angular range provided the best CNRs, probably because the large-angle PVs can better separate overlapping in the depth direction and thus enhance the object contrast in the reconstruction. All CNR results from the subsets were inferior to those from the full set.

The line profiles and the ASF curves of the low-contrast mass were shown in Figures 3 and 4, respectively. The results of the high-contrast mass were not shown but have similar behavior. There is no obvious difference among the normalized line profile of masses from the six subsets, probably because the line profiles of relatively low contrast objects are not sensitive to in-plane blurring due to the subset sampling. The UN sampling, which had the narrowest angular range (±15º) among all conditions, gave much worse ASF behavior than others. Among the rest, the NCD sampling, which had slightly narrower angular range (±27º) than others of full range (±30º), gave slightly worse ASF. In other words, interplane blurring of mass depended strongly on the total angular range. The NED sampling, which had all 10 PVs evenly distributed on extreme sides in addition to one in the middle, yielded the best ASF or least interplane blurring, even slightly better than the full set result. This is probably because the PVs in-between, especially those close to the middle region, contribute more blurring to the out-of-focus planes than the extreme PVs.

The normalized in-plane and interplane line profiles of the high-contrast wire were shown in Figures 5 and 6, respectively. Different from the simulated low-contrast mass, the UN result provided the best in-plane sharpness while the NED sampling worst. This is because the extreme side PV distributions did not provide enough information to reconstruct the high-contrast wire on the in-focus plane, thus reducing the sharpness. On the other hand, based on the similar reason we discussed about simulated masses, the NED sampling provided the narrowest ASF and thus least interplane blurring for the high-contrast wire.

In addition to the phantom study, a DBT patient case was reconstructed with the six subset sampling and the full-set of PVs. An ROI containing a spiculated mass was extracted for comparison. Figure 7 shows the ROIs from the middle PV image and from a DBT slice intersecting approximately the center of the mass reconstructed under each of the conditions. It can be seen that on the middle PV image, the mass boundary and the spiculations appear to be blurred due to the overlapping tissues. The full-set reconstruction results in the best image quality with sharp speculations, and the breast parenchyma is reasonably free of artifacts. In comparison, the UN subset yields relatively sharp spiculations but there are additional structures on the image that may be caused by overlapping tissues from the reduced depth resolution. The spiculations and edges from the UW subset are slightly more blurred than those from the UN subset but the background exhibits less structures. The NCD, NCS and NES

subsets provide comparable spiculations. The NED subset results in the worst spiculation details and most blurred mass margins. The textural artifacts in the background tissue from the NCD, NCE, NED, NES subsets are worse than those from the UN and UW subsets in some regions.

4 Discussion

DBT mammography can provide quasi-3D information of the breast in contrast to conventional mammography. With a breast phantom study, we compared results of six subset samplings of 11 PVs out of the 21 original PVs and the results of the full set of 21 PVs. Preliminary results demonstrated that the larger the DBT angular range, the better the CNR and ASF of simulated masses. In case of equivalent angular range, PVs acquired at large projection angles had stronger effect on depth resolution than those close to the middle region. For a high-contrast wire, a narrower angular range led to shaper in-plane edge and the PVs acquired at large projection angles reduced the blurring of inter-plane profile. No subset was superior to the others in all performance measures, indicating the inevitable tradeoff between in-plane resolution and depth resolution. The tradeoff is less clear for the DBT images of a spiculated breast mass. The overlapping tissue causes structural textures on the reconstructed slices. The full set reconstruction demonstrates a clear advantage in terms of in-plane and depth resolutions. The superior image quality can be partly attributed to the higher dose with the use of all 21 PVs. The comparison of the PV distribution in the full set with those of the other six subsets is therefore not completely fair unless we can keep the total dose of the set of PVs at a constant level. Due to restrictions on the unit required for other clinical evaluations, our DBT system is not enabled to acquire PV images of different dose distributions. However, it has been suggested that higher dose acquisition in some specific PVs than others might improve image quality. We will include this non-uniform dose approach in future studies if advanced system operating modes become available or by using computer simulations.

Acknowledgments. This work is supported by U. S. Army Medical Research and Materiel Command grant W81XWH 07-1-0324, and USPHS grants CA120234, CA91713 and CA95153. The digital breast tomosynthesis system was developed by the GE Global Research Group through the Biomedical Research Partnership (USPHS grant CA91713, PI: Paul Carson, Ph.D.) collaboration.

References

1. Niklason, L. T., Christian, B. T., Niklason, L. E., et al.: Digital tomosynthesis in breast imaging. Radiology 205, 399-406 (1997).
2. Wu, T., Stewart, A. Stanton, M., et al.: Tomographic mammography using a limited number of low-dose cone-beam projection images. Medical Physics 30, 365-380 (2003).
3. Kopans, D.: Digital tomosynthesis and other applications. RSNA Program Book, 130 (2005).

4. Helvie, M. A., Roubidoux, M. A., Hadjiiski, L. M., Zhang, Y., Carson, P. L., and Chan, H.-P.: Tomosynthesis Mammography vs Conventional Mammography: Comparison of Breast Masses Detection and Characterization. RSNA Program Book, 381 (2007).
5. Eberhard, J. W., Staudinger, P., Smolenski, J., et al.: High speed, large angle mammography tomosynthesis system. Proc. SPIE 6142, 61420C (2006).
6. Zhang, Y., Chan, H.-P., Sahiner, B., et al: A comparative study of limited-angle cone-beam reconstruction methods for breast tomosynthesis. Medical Physics 33, 3781-3795 (2006).
7. Andersen, A. H., and Kak, A. C.: Simultaneous algebraic reconstruction technique (SART): a new implementation of the ART algorithm. Ultrason. Imaging 6, 81-94 (1984).

Table 1. Projection angles (in degrees) of the six different sampling of PVs.

Uniform-Narrow (UN)	±15	±12	±9	±6	±3	0
Uniform-Wide (UW)	±30	±24	±18	±12	±6	0
Nonuniform-Central-Dense (NCD)	±27	±18	±9	±6	±3	0
Nonuniform-Central-Sparse (NCS)	±30	±21	±12	±6	±3	0
Nonuniform-Extreme-Sparse (NES)	±30	±27	±24	±6	±3	0
Nonuniform-Extreme-Dense (NED)	±30	±27	±24	±21	±18	0

Table 2. The contrast-to-noise ratio (CNR) results of the selected masses.

	UN	NCD	NES	NCS	UW	NED	FS
Angular range	±15	±27			±30		
# PVs outside ±6°	6	6	6	6	8	10	16
Low-contrast mass	2.85	3.56	3.68	3.88	4.13	4.05	4.74
High-contrast mass	6.36	7.37	7.51	7.85	8.27	8.28	9.47

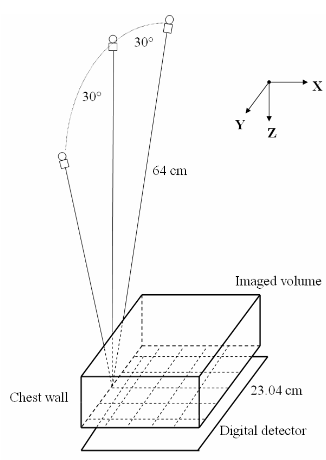

Fig. 1. Geometry of the GE GEN2 digital breast tomosynthesis mammography system.

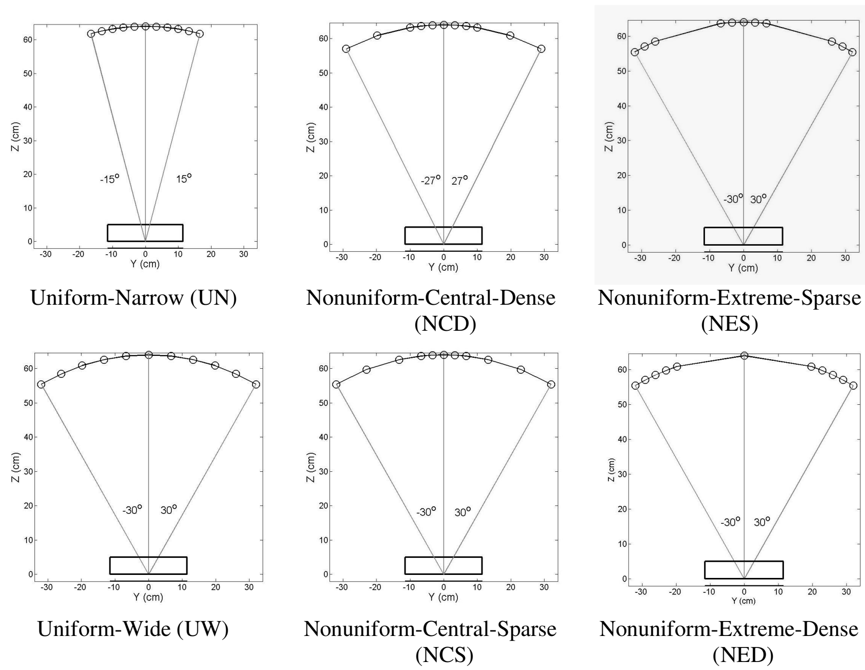

Uniform-Narrow (UN)

Nonuniform-Central-Dense (NCD)

Nonuniform-Extreme-Sparse (NES)

Uniform-Wide (UW)

Nonuniform-Central-Sparse (NCS)

Nonuniform-Extreme-Dense (NED)

Fig. 2. Six different distributions of PV images.

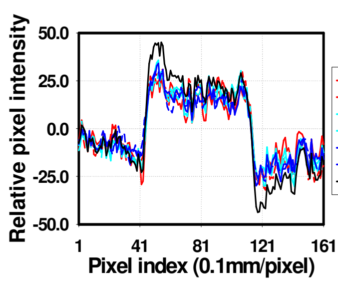

Fig. 3. Normalized in-plane line profiles of the selected low-contrast mass for different subsets of PVs and the full set.

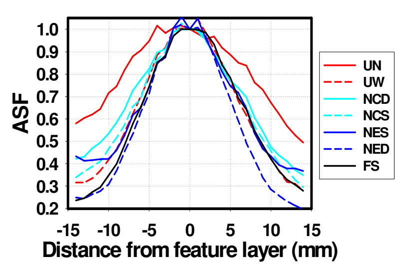

Fig. 4. ASF of the selected low-contrast mass with different subsets and the full set.

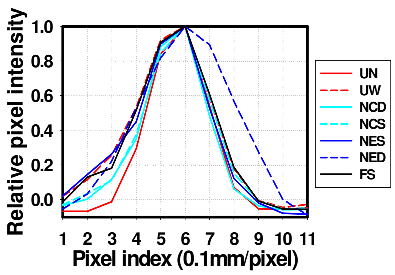

Fig. 5. Normalized in-plane line profiles of the selected wire.

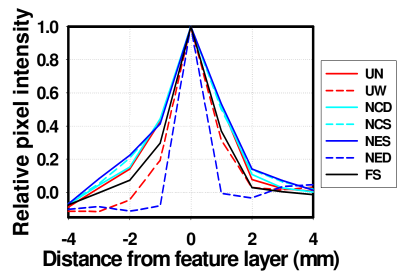

Fig. 6. Normalized inter-plane line profiles along Z-axis of the selected wire.

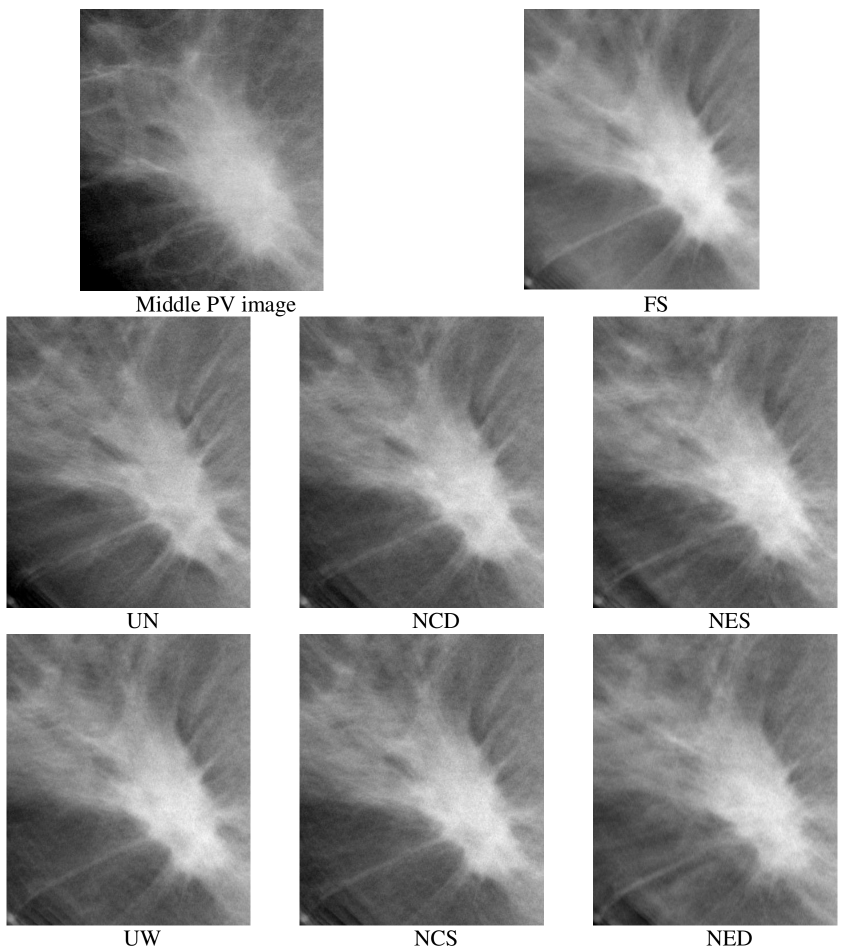

Fig. 7. Spiculated mass of the selected patient DBT case on projection view image (0 degree) and reconstructions under the full set and the six subset sampling conditions.